Excitonic effects at the temperature-dependent E_1 and $E_1 + \Delta_1$ critical points of Ge

C. A. Armenta* and S. Zollner

Department of Physics, New Mexico State University, MSC 3D, P. O. Box 30001, Las Cruces, NM 88003-8001, USA

(*Electronic mail: cobhc14@nmsu.edu.)

(Dated: 3 June 2025)

We investigated excitonic effects in the complex dielectric function of Ge near the E_1 and $E_1 + \Delta_1$ critical points as a function of temperature. By employing Tanguy's theory for two-dimensional excitons [C. Tanguy, Solid State Commun. 98, 65 (1996)], we fitted the second derivative of the dielectric function to a temperature series of spectroscopic ellipsometry measurements ranging from 4 K to 800 K [C. Emminger *et al.*, J. Vac. Sci. Technol. B 38, 012202 (2020)]. We analyzed the temperature dependence of the effective masses, matrix elements, and exciton binding energies to develop a model for the dielectric function that requires no fitting parameters, apart from energy and broadening. Our calculations not only show a remarkable agreement between theory and experiment, but also provide a model for the absorption by two-dimensional excitons that can be adapted to other applications and materials.

I. INTRODUCTION

Basic optical processes like the absorption or emission of photons and the creation and recombination of electron-hole pairs are discussed qualitatively in reference to experimental results in many popular textbooks, $^{1-3}$ but a quantitative comparison of theory and experiment has long been elusive. Progress has been made recently by describing the local electronic band structure using $\mathbf{k} \cdot \mathbf{p}$ -theory and the Coulomb interaction between the electron and hole with the Elliott-Tanguy theory of excitons. This formalism has been applied to the direct and indirect gap absorption in Ge and the lineshape of the photoluminescence of Ge as a function of temperature.

The present manuscript applies the same formalism to the prominent E_1 and $E_1 + \Delta_1$ peaks in the complex dielectric function of Ge. Our results are predictive, because only known parameters (such as band gaps and effective masses) are used to calculate the strength of the optical absorption. They can therefore be applied universally to many different diamond and compound semiconductors, including semiconductor alloys important for electronic and optoelectronic applications.

II. TWO-DIMENSIONAL EXCITONS

The electronic band structure of Ge presents two van Hove singularities in the [111]-direction (Λ) of the wave vector **k** in the Brillouin zone (see Fig. 1b). These critical points (CPs) arise due to the conduction band (CB) running parallel to the valence band (VB) over a certain range of **k**-vectors. Labeled as E_1 and $E_1 + \Delta_1$, these CPs are transitions occurring from the heavy-hole (hh) and light-hole (lh) VBs to the CB, respectively. Categorized 1.9 as a two-dimensional minimum critical point M_0 , the literature gives the dielectric function (DF) versus photon energy $\varepsilon(E)$ for such CPs as $^{10-14}$

$$\varepsilon(E) = C - Be^{i\phi} \ln(E - E_1 + i\Gamma), \tag{1a}$$

with
$$\frac{\mathrm{d}^2 \varepsilon(E)}{\mathrm{d}E^2} = \frac{B e^{i\phi}}{\left(E - E_1 + i\Gamma\right)^2}.$$
 (1b)

In CP analysis, typically only Eq. (1b) is fitted to the data with amplitude B, phase angle ϕ , energy E_1 , and broadening Γ as its free parameters. ¹⁵ Variable C in Eq. (1a) is a constant. Unfortunately, this type of analysis only provides information about the energy and broadening for the structures of interest, while leaving the form of the DF without an accurate description. Eq. (1a) does not yield a good description of the dielectric function or the CP parameters. ¹⁶

Conversely, in cases where the calculation of the DF has been attempted, the description of this CP lineshape has been limited to a qualitative discussion. 17,18 A major pitfall in these calculations is the omission of the Coulomb interaction between the electrons excited to the CB and the holes left in the VB. These electron-hole pairs tend to form excitons (bound together in a hydrogen-like system). Because of the joint (JDOS) of these transitions, the excitonic systems for E_1 and $E_1 + \Delta_1$ are confined to a two-dimensional plane. Equation (2) shows the JDOS for the E_1 CP in a coordinate system where the *z*-axis points along the [111]-direction. Naturally, in this coordinate system, the *x*- and *y*-axis would be along the [1 $\overline{10}$]-and [11 $\overline{2}$]-direction, respectively.

$$J_{\rm CV}(E) \propto \int \frac{\mathrm{d}\mathbf{k}}{8\pi^3} \delta \left[E_1 + \frac{\hbar^2}{2} \left(\frac{k_x^2 + k_y^2}{\mu_\perp} + \frac{k_z^2}{\mu_\parallel} \right) - E \right]. \quad (2)$$

The longitudinal reduced effective mass μ_{\parallel} in Eq. (2) is significantly greater than the transverse reduced effective mass μ_{\perp} .¹⁸ As a result, the JDOS effectively confines the motion of the exciton to the *x*-*y* plane, as depicted in Fig. 1a.

In essence, an accurate description of the aforementioned CPs must take into account the effects of the formation of these quasi-two-dimensional excitons. In recent years, great progress has been made in the implementation of the *GW*-method and the Bethe-Salpeter equations (BSE) to calculate

the DF of different semiconductors. ^{19–21} This approach accounts for excitons by making quasi-particle energy corrections to the initial density functional theory calculations of the band structure. It also accounts for the Sommerfeld enhancement of excitonic absorption over the absorption by uncorrelated electron-hole pairs. Barker *et al.*, ²⁰ for instance, correctly resolve the E_1 and $E_1 + \Delta_1$ CPs in the DF of GaSb. Unfortunately, this approach requires a significant amount of computing time and provides only limited agreement when compared with experiment. Instead, we aim to provide a closed-form expression for the DF that can easily be implemented on a personal computer.

Culminating prior efforts of finding a solution to this problem, ^{22,23} Tanguy provided an expression for the complex DF that incorporates the effects of two-dimensional Wannier excitons.²⁴ Unlike GW-BSE, which requires large computational resources and provides only an approximation to the DF, Tanguy's model offers a fully analytical solution.²⁴ This allows for direct comparison with experimental data without the need for extensive numerical fitting. Still, despite Tanguy's work being published almost three decades ago,²⁴ comparison of theory with experiment is lacking in the literature. In the present work, we will bridge this gap by comparing Tanguy's model to the DF of Ge near the E_1 and $E_1 + \Delta_1$ CPs. This model not only provides a better description of the DF than previous attempts, but also requires no fitting parameters apart from energy and broadening. Furthermore, having a reduced number of fitting parameters makes this model highly applicable to other areas of research, such as the description of band-filling effects^{25,26} and ultrafast phenomena.^{27–29} Because of its compact form, the model can also be applied to other semiconductor materials of interest, such as InSb, GaAs, and $Ge_{1-x}Sn_x$ alloys.

For comparison with experiment, we used data published by Emminger *et al.*,³⁰ which comprises a temperature series of spectroscopic ellipsometry measurements, ranging from 4 to 800 K. We will briefly discuss the acquisition, reduction, and modeling of the data. We will also analyze Tanguy's DF expression, as well as how it can be adapted to the material of interest. The fixed parameters of the model tend to change with temperature, hence we will discuss the temperature dependence of both, the fixed and free parameters. Finally we will point out the shortcomings of the model and how they can be improved upon.

III. EXPERIMENTAL DATA

The experimental data consist of spectroscopic ellipsometry measurements of a wafer of bulk Ge with (100) surface orientation. With a separation of 10 meV, the data collected ranged from 0.7 to 6.3 eV. There were a total of 32 measurements ranging from 4 to 800 K. We will not discuss the details of these measurements any further. If interested in more information about the cleaning procedure, acquisition settings, and temperature control methods, we encourage the reader to look at the original publication.³⁰

What is relevant for our purposes is the effect of the na-

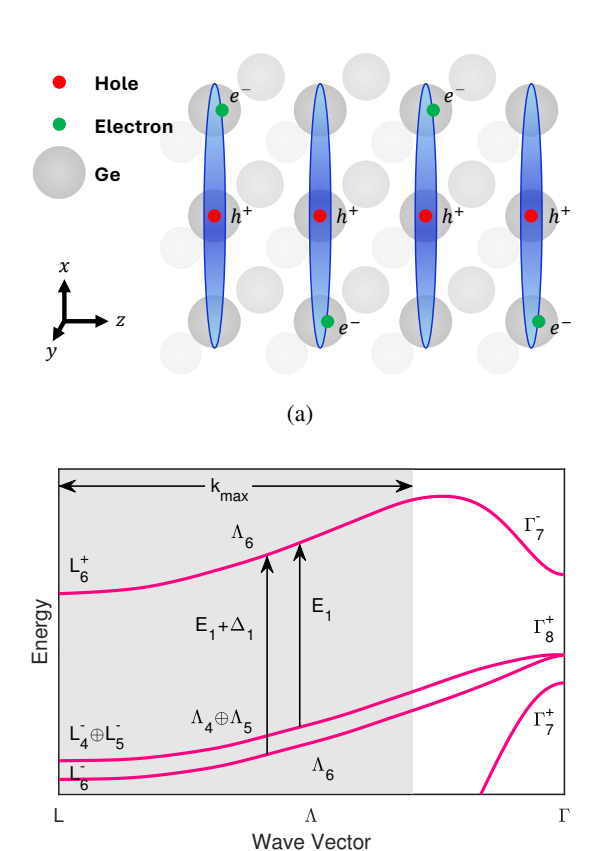


FIG. 1: (a) Because the longitudinal reduced mass μ_{\parallel} is much larger than the transverse reduced mass μ_{\perp} in the CPs E_1 and $E_1 + \Delta_1$, the excitons are restricted to the plane perpendicular to the z-axis. (b) Band structure of Ge in the Λ -direction, where the E_1 and $E_1 + \Delta_1$ transitions (black arrows) are located. The range of wave vectors \mathbf{k} where these transitions take place is labeled k_{max} (grey region).

(b)

tive oxide layer embedded in the data. Because we are interested in only the bulk material, it is necessary to correct for the oxide overlayer that is present at the moment of the measurement. To make this oxide correction, we can use the optical properties of GeO₂ published by Nunley et al.³¹ The procedure consist of simulating the pseudo-DF using Nunley's GeO₂ and Emminger's parametric semiconductor oscillator models.^{30,31} In this manner, we construct a point-by-point fit that extracts the DF of the bulk material and removes any effects from the oxide layer. We achieved this with the aid of the commercial software WVASE32, from the J. A. Woollam company.³² We note that the oxide layer thickness varied slightly at each temperature. Therefore, there could be small errors in the layer thickness estimated by this oxide correction. If the wrong oxide thickness is used, it could lead to surface effects that will affect the amplitude of the imaginary part of the DF. We will expand on these surface effects in Sec. VI.

IV. TANGUY MODEL

At a two-dimensional CP with energy E_1 , Tanguy²⁴ provides the optical dispersion for a two-dimensional exciton by incorporating broadening to both, the continuum and discrete absorption spectra. This complex DF is given by²⁴

$$\varepsilon(E) = \frac{A}{\pi (E + i\Gamma)^2} \left\{ g_a \left[\xi(E + i\Gamma) \right] + g_a \left[\xi(-E - i\Gamma) \right] - 2g_a \left[\xi(0) \right] \right\}, \tag{3}$$

where

$$A = \frac{e^2 \mu_{\perp} |\mathbf{e} \cdot \mathbf{M}_{\text{CV}}|^2}{\pi \varepsilon_0 m_0^2}, \, \xi(z) = \sqrt{\frac{R}{E_1 - z}}, \tag{4a}$$

and
$$g_a(\xi) = 2\ln(\xi) - 2\psi\left(\frac{1}{2} - \xi\right)$$
. (4b)

In Eq. (4a), the amplitude A depends on the electron charge e, the free electron mass m_0 , the permeability of free space ε_0 , the reduced mass of the two-dimensional exciton μ_\perp , and the transition matrix element $\mathbf{e} \cdot \mathbf{M}_{\text{CV}}$, whereas the argument ξ depends on the exciton's binding energy R and the CP energy E_1 . In Eq. (4b), $\psi(z)$ is the complex digamma function

$$\psi(z) = \frac{\mathrm{d}}{\mathrm{d}z} \ln \Gamma(z) = \frac{\mathrm{d}}{\mathrm{d}z} \ln \left(\int_0^\infty t^{z-1} e^{-t} \mathrm{d}t \right), \tag{5}$$

where $\Gamma(z)$ is the complex gamma function. In the case of the CPs E_1 and $E_1 + \Delta_1$ of Ge, we can replace the amplitude in Eq. (3) with 17,25,26

$$A^{(E_1)} = \frac{4e^2 \mu_{\perp}^{(E_1)} \overline{P}^2}{3\pi \varepsilon_0 m_0^2} k_{\text{max}} \text{ for } E_1$$
 (6a)

and
$$A^{(E_1+\Delta_1)} = \frac{4e^2\mu_{\perp}^{(E_1+\Delta_1)}\overline{P}^2}{3\pi\varepsilon_0 m_0^2} k_{\text{max}} \text{ for } E_1 + \Delta_1,$$
 (6b)

where $\mu_{\perp}^{(E_1,E_1+\Delta_1)}$ are the transverse reduced masses of the CPs, \overline{P} is the average transition matrix element, and k_{\max} is the maximum range along the k_z -axis where interband transitions take place. For details about these amplitudes, refer to the supplementary material Sec. S2. Previous calculations of the DF for these CPs neglected the correlation between electrons and holes, resulting in a step-like function^{17,18,25,26} [see Eq. (S15) in Sec. S2 of the supplementary material for details on this step function].

To illustrate these excitonic effects, Fig. 2 shows the comparison between the DF for uncorrelated electron-hole pairs (blue dashed line) and the two-dimensional excitonic line-shape (black solid line). Fig. 2 also shows the two components of Eq. (3), the continuum and discrete absorption (shown by the red and green dot-dashed lines, respectively). Fig. 2 shows that the DF for the uncorrelated electron-hole pairs is almost identical to the exciton continuum absorption spectra. We also observe that the peak absorption occurs at an energy equal to $E_1 - R(1)$ for 22,33,34

$$R(n) = \frac{\mu_{\perp}}{m_0 \varepsilon_{\text{st}}^2 \left(n - \frac{1}{2}\right)^2} \text{Ry, where } n = 1, 2, 3, ...,$$
 (7)

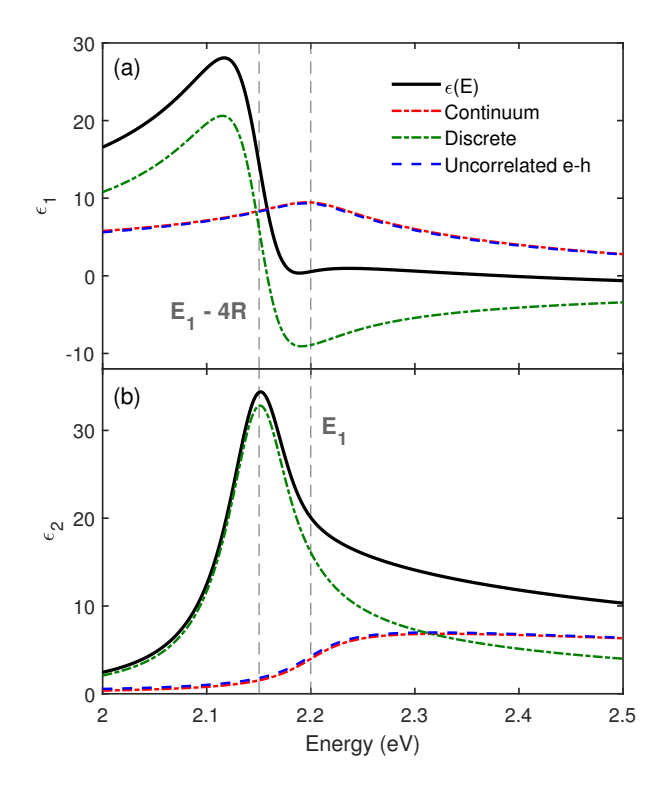


FIG. 2: (a) Real and (b) imaginary part of the dielectric function of two-dimensional Wannier excitons. This complex dielectric function (solid black line) is composed of the continuum (red dot-dashed line) and bound states (green dot-dashed line) of the exciton. Notice the similarity between the continuum state and the optical dispersion for uncorrelated electronhole pairs (blue dashed line). The arbitrary values for the parameters are $E_1 = 2.2$ eV, $\Gamma = 37$ meV, and A = 41.8 eV².

 $\varepsilon_{\rm st}$ is the static dielectric constant, and Ry = 13.6 eV is the Rydberg energy constant. Equation (7) gives the binding energy of the 2D exciton, which is the same as for a 2D hydrogen-like system. ^{22,33,34} Fig. 2 also shows how the oscillator strength in the imaginary part of the DF is enhanced significantly by the discrete (bound exciton) absorption. This is a typical behavior of not only two-dimensional M_0 excitons in bulk materials, ¹ but also of excitonic absorption in two-dimensional materials, where the reduced dimensionality enhances the Coulomb interaction due to the confinement of the carriers. ^{23,35,36}

A. Temperature dependence of the fixed parameters

As previously stated, other than energy and broadening, Eq. (3) combined with the amplitudes in Eq. (6), provides a model absent of any fitting parameters for the CPs near the L-valley of Ge. The matrix element $E_P = \overline{P}^2/m_0$ and the static dielectric constant $\varepsilon_{\rm st}$ have well established values in the literature. 7.25,37,38 Another required parameter is $k_{\rm max}$. In the rotated coordinate system, the total distance from Γ to L along

the k_z -axis (the Λ -direction) is $\pi\sqrt{3}/a_0$. Under visual inspection, however, the $k_{\rm max}$ value lies between $3\pi\sqrt{3}/(5a_0)$ and $3\pi\sqrt{3}/(4a_0)$. Therefore, for our purposes, we allowed the $k_{\rm max}$ parameter to vary within this range, but kept it fixed across all temperatures. Since we are interested in the temperature effects of the DF, we can follow the procedure described by Emminger *et al.*⁶ to incorporate the temperature dependence of the lattice constant, and dielectric constant in the following manner:

$$a_0(T) = a_0(0 \text{ K}) + \frac{1.315 \times 10^{-2} \text{ Å}}{\exp[(355.14 \text{ K})/T] - 1},$$
 (8)

$$E_P(T) = E_P(0 \text{ K}) \frac{a_0(0 \text{ K})^2}{a_0(T)^2},$$
 (9)

$$\varepsilon_{\rm st}(T) = 1 + \left[\frac{15.6 \text{ eV}}{E_{\rm Penn}(T)} \right]^2. \tag{10}$$

The term $E_{\text{Penn}}(T)$ in Eq. (10) is the Penn gap given by 1,6

$$E_{\text{Penn}}(T) = 4.146 \text{ eV} - (0.05 \text{ eV}) \left[\frac{2}{e^{(217 \text{ K})/T} - 1} + 1 \right].$$
 (11)

For the values at zero temperature, $E_P(0 \text{ K}) = 12.96 \text{ eV}^{7.25}$ and $a_0(0 \text{ K}) = 5.6516 \text{ Å}.^{40}$

B. Unrenormalized effective mass

Yet another required parameter is the transverse reduced mass μ_{\perp} , which is needed to calculate the exciton binding energy using Eq. (7), as well as the amplitudes in Eq. (6). While Dresselhaus *et al.* determined the effective electron mass $m_{\perp}{=}0.082$ of the CB from cyclotron resonance measurements, ⁴¹ to calculate μ_{\perp} , we also require explicit values for the effective masses of the heavy and light holes at the L-valley, for which reliable values are not available. Menéndez *et al.* provide the reduced masses for both CPs as ⁷

$$\frac{1}{\mu_1^{(E_1)}} = \frac{E_P}{m_0} \left[\frac{2}{E_1^u} + \frac{1}{(E_1 + \Delta_1)^u} \right],$$
 (12a)

and
$$\frac{1}{\mu_{\perp}^{(E_1 + \Delta_1)}} = \frac{E_P}{m_0} \left[\frac{1}{E_1^u} + \frac{2}{(E_1 + \Delta_1)^u} \right].$$
 (12b)

These expressions come from a 6-band $\mathbf{k} \cdot \mathbf{p}$ -theory model (see supplementary materials Sec. S1 A for a derivation). In Eqs. (12), however, one must be careful with the energy values of E_1 and $E_1 + \Delta_1$. Zollner *et al.*⁴² point out that to calculate the effective mass, one must use the unrenormalized energy values, rather than the experimental energies of the CPs. This is

the meaning of the superscripts u. The unrenormalized values of the CPs incorporate the redshift due to thermal expansion, but not the self-energy due to the deformation-potential electron-phonon coupling. We can obtain the unrenormalized energy as a function of temperature with the expression

$$E_{E_1,E_1+\Delta_1}^u(T) = E_{E_1,E_1+\Delta_1}^u(0 \text{ K})$$
$$-3B\left(\frac{\partial E_{E_1,E_1+\Delta_1}^{\text{exp}}}{\partial p}\right)_T \int_0^T \alpha(\theta) d\theta, \quad (13)$$

where $\alpha(T)$ is the temperature-dependent thermal expansion coefficient, $B=7.58\times 10^{10}$ Pa is the bulk modulus, ⁴³ and $(\partial E_{E_1}^{\rm exp}\Big/\partial p)_T=7.5\times 10^{-6}~{\rm eV\cdot cm^2\cdot kg^{-1}}$ is the pressure coefficient of the E_1 CP. ⁴⁴ For this calculation, we take the value of $(\partial E_1/\partial p)_T\approx [\partial (E_1+\Delta_1)/\partial p]_T$. We justify this assumption by noting that the spin-orbit splitting Δ_1 is related to atomic effects and it is, for the most part, unaffected by the distance of the atoms within the lattice. The thermal expansion coefficient ⁴⁵

$$\alpha(T) = \frac{1}{a_0(T)} \frac{\mathrm{d}a_0(T)}{\mathrm{d}T},\tag{14}$$

can be calculated from the expression for the lattice constant in Eq. (8). Finally, the unrenormalized energy at zero temperature can be obtained by the following procedure: We first determine experimentally the energy of the CPs as a function of temperature. These data points are then fitted with a Bose-Einstein (BE) model¹³

$$E_{E_1,E_1+\Delta_1}(T) = E_a - E_b \left(1 + \frac{2}{e^{\theta_B/T} - 1}\right).$$
 (15)

Once the fitted parameters E_a , E_b , and θ_B are determined, we set $E^u_{E_1,E_1+\Delta_1}(0 \text{ K})=E_a$, where the parameter E_a differs for each CP. Since we do not know the value of E_a a priori, we used the experimental value $E^{\text{exp}}_{E_1,E_1+\Delta_1}(0 \text{ K})$ from Ref. 14 as a starting point for the fit. We then refitted the data using the updated value of E_a obtained from the previous iteration. This process was repeated iteratively until E_a converged to a constant value.

C. Complete model

To encompass both CPs, we added two expressions similar to Eq. (3) with the appropriate amplitudes and binding energies for E_1 and $E_1 + \Delta_1$. We also added a constant offset ε_{off} to the real part of the DF, to account for additional nonresonant contributions from other interband transitions. The complete form of our model is

$$\varepsilon(E) = \varepsilon_{\text{off}} + \frac{A^{(E_{1})}}{\left[E + i\Gamma^{(E_{1})}\right]^{2}} \left\{ g_{a} \left[\sqrt{\frac{R^{(E_{1})}}{E_{1} - E - i\Gamma^{(E_{1})}}} \right] + g_{a} \left[\sqrt{\frac{R^{(E_{1})}}{E_{1} + E + i\Gamma^{(E_{1})}}} \right] - 2g_{a} \left[\sqrt{\frac{R^{(E_{1})}}{E_{1}}} \right] \right\} + \frac{A^{(E_{1} + \Delta_{1})}}{\left[E + i\Gamma^{(E_{1} + \Delta_{1})}\right]^{2}} \left\{ g_{a} \left[\sqrt{\frac{R^{(E_{1} + \Delta_{1})}}{E_{1} + \Delta_{1} - E - i\Gamma^{(E_{1} + \Delta_{1})}}} \right] + g_{a} \left[\sqrt{\frac{R^{(E_{1} + \Delta_{1})}}{E_{1} + \Delta_{1} + E + i\Gamma^{(E_{1} + \Delta_{1})}}} \right] - 2g_{a} \left[\sqrt{\frac{R^{(E_{1} + \Delta_{1})}}{E_{1} + \Delta_{1}}}} \right] \right\}.$$
(16)

It is worth pointing out that, in the parabolic approximation of the reduced masses of Eq. (12), the matrix element E_P cancels out in the amplitudes of Eq. (6). The resulting amplitudes have the form

$$A^{(E_1)} = \frac{4e^2 E_1^u (E_1 + \Delta_1)^u k_{\text{max}}}{3\pi\varepsilon_0 \left[2(E_1 + \Delta_1)^u + E_1^u\right]} \text{ for } E_1 \qquad (17a)$$
and
$$A^{(E_1 + \Delta_1)} = \frac{4e^2 E_1^u (E_1 + \Delta_1)^u k_{\text{max}}}{3\pi\varepsilon_0 \left[(E_1 + \Delta_1)^u + 2E_1^u\right]} \text{ for } E_1 + \Delta_1. \tag{17b}$$

With this definition, the ratio of the CPs amplitudes would be $A^{(E_1)}/A^{(E_1+\Delta_1)} \propto (3E_1+\Delta_1)/(3E_1+2\Delta_1)$, or about 0.97 for a temperature of 4 K.

V. RESULTS

A. Fitting procedure

To fit the energy and broadening parameters, we performed a CP analysis by fitting the 2nd derivative of our model in Eq. (16) to the 2nd derivative of the experimental data. We then compared their respective DFs. To obtain the 2nd derivatives, we applied a digital filter to the DF to smooth the original signal and suppress the noise in the experimental data. We then convoluted the DF with the derivative of the filter to obtain the desired DF derivative (see Sec. S4 for more information on this procedure). For the digital filter, we used the extended Gauss (EG) filter, which is defined in direct space as 46,47

$$b_M(x) = \sum_{m=0}^{M} \left[(-1)^m \frac{\Delta E^m}{m!} \frac{\mathrm{d}^m}{\mathrm{d}\Delta E^m} \right] \frac{\exp\left[-x^2/(4\Delta E^2)\right]}{2\sqrt{\pi \Delta E}}, (18)$$

where we selected M=4 according to the discussion in Ref. 46. The filter width ΔE was determined by identifying the white noise onset in the Fourier coefficients of the data.⁶ In general, given that noise increases with temperature, the selected filter width also increased accordingly. To fit our model parameters, we minimized the residuals between the DF derivatives of the experimental data and the model. We performed this minimization procedure using MATLAB's nonlinear least-squares optimization function.⁴⁸ For consistency, the derivative of the model must be computed in the same manner as the derivative of the experimental data.¹⁶ Therefore, we convoluted Eq. (16) with the same EG filter (and

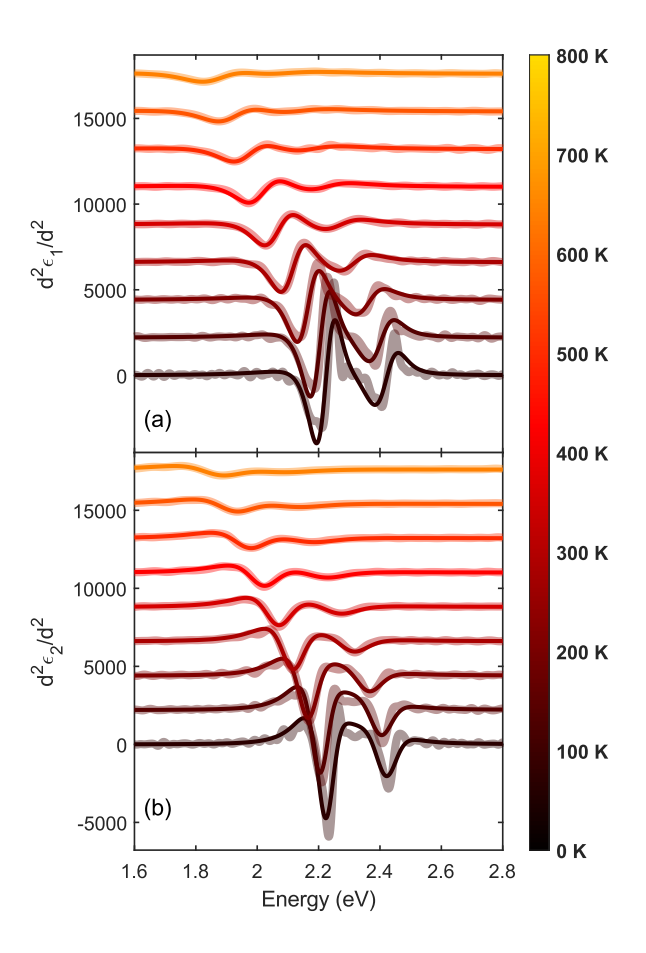


FIG. 3: 2nd derivative of the real (a) and imaginary (b) part of the dielectric function. The derivatives of the experimental data (translucent lines) were calculated using the EG digital filter in Eq. (18). The fitted 2nd derivatives of Eq. (16) for each temperature are shown by the solid lines.

same filter width ΔE) while leaving the fitting parameters free. Fig. 3 shows that the fitted derivative of the model is in good agreement with the experimental data.

To make the critical point analysis more thorough, we repeated the minimization procedure with a Savitzky-Golay (SG) digital filter.⁴⁹ To generate the smoothing filter, we used

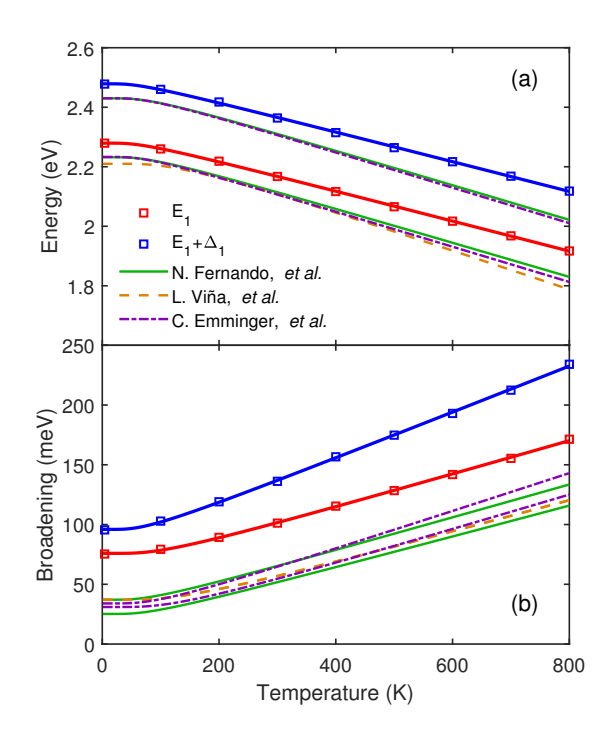


FIG. 4: Bose-Einstein model fits for the energy (a) and broadening (b). Shown by the squares are the fitted parameters, while the blue and red solid lines are the Bose-Einstein models. For comparison, data from different references is also shown. ^{13,14,30}

MATLAB's SG built-in function.⁴⁸ The order of the polynomial to be fitted was selected according to the noise of the data. Again, similar to the EG filter, the order of the polynomial needed to be adjusted at each temperature. The frame length, on the other hand, was constrained to 5% of the total number of data points. The results were nearly identical to the EG digital filter. The values of the fitted parameters varied less than 1% between the two digital filters. Hence, the derivatives for the SG filter are not shown in Fig. 3. For a more in-depth discussion of the fitting procedure and comparison of the two digital filters, see Sec. S4 in the supplementary material.

B. Temperature dependence of the fitting parameters

We can use the fitted energies and broadenings of the entire temperature series to characterize these parameters as a function of temperature. We do this by fitting the BE model of Eq. (15) and (19) to the energy and broadening parameters:¹³

$$\Gamma^{(E_1, E_1 + \Delta_1)}(T) = \Gamma_1 + \Gamma_0 \left(1 + \frac{2}{e^{\theta_B/T} - 1} \right).$$
 (19)

The squares in Fig. 4 show the fitted parameters from the 2nd derivative analysis. Along with the BE models of the present work, Fig. 4 also shows the BE models for these CPs from the literature for comparison. ^{13,14,30} It is clear from Fig. 4 that the

energies of our model are greater than in the previous characterization efforts. This is to be expected, since the fitted absorption maximum in our model is not the energy of the CP, but rather the first discrete absorption peak of the exciton, which is lower than the CP energy by the exciton binding energy. Broadening also behaves differently. In Refs. 13,14,30, the broadenings of the CPs are fitted with Eq. (1b). In contrast, Eq. (3) incorporates broadening by convolution with a Lorentzian. Although they are difficult to compare quantitatively given the two extra parameters B and ϕ , the broadening of Eq. (1b) tends to be larger than for a Lorentzian oscillator. Thus, our model requires a larger broadening than the references values to match the experimental data. Table I shows the fitted parameters for the BE model, along with the parameters in the literature.

C. Dielectric function

At a temperature of 4 K, Fig. 5 shows the model DF (16) in comparison to the experimental data. Fig. 6 shows the same comparison for temperatures from 100 to 600 K. These figures show an outstanding agreement between the theoretical model and the experimental DF across the entire temperature range. This level of agreement is remarkable given that no free parameters other than energy and broadening are fitted. Nonetheless, it is evident from Figs. 5 and 6 that, while the model is in excellent agreement with the data near the CPs, it misses contributions from additional absorption processes. At lower energies, the model underestimates the value of ε_2 by about 2 units. We attempted to reduce this mismatch by including the direct bandgap absorption of Ge. At around 0.9 eV, the direct bandgap of Ge E_0 presents itself as the first CP contributing to the absorption. The DF near E_0 is categorized as a three-dimensional M_0 van Hove singularity. A description of this CP that not only accounts for the formation of excitons, but also incorporates excitonic screening already exists in the literature.^{5,50} More importantly for our purposes, this lineshape has previously been applied to Ge in a temperature series similar to our data.⁶ In their approach, Emminger et al.⁶ used the experimental, rather than the unrenormalized E_0 CP energies for the calculation of the effective masses. Unfortunately, even with the corrected energies and incorporating non-parabolicity effects, E_0 contributes less than 1 unit to the amplitude of ε_2 . Therefore, we did not include the CP E_0 in our calculations (see supplementary material Sec. S5 more information on E_0). The E_0' and E_2 CPs also contribute to ε_2 at higher energies. However, unlike the direct bandgap E_0 , there is no established lineshape for these CPs, hence these contributions to the absorption are omitted as well.

A more significant issue than the mismatch at high and low energies is the deviation of ε_2 at E_1 (around 2.2 eV) and $E_1+\Delta_1$ (around 2.4 eV). At the E_1 CP, the ε_2 amplitude of our model is smaller than in the experimental data, whereas for $E_1+\Delta_1$, the model overestimates the amplitude. This could be due to an incorrect value of $k_{\rm max}$, which has been fixed at $0.7\pi\sqrt{3}/a_0$ for all our calculations. As seen in Fig. 1b, the range over which the hh-band ($\Lambda_4 \oplus \Lambda_5$ -band) is parallel

TABLE I: Fitted parameters of the Bose-Einstein model for the energy and broadening of the E_1 and $E_1 + \Delta_1$ critical points.

	E_a (eV)	E_b (eV)	$\theta_{B_E}(K)$	Γ ₁ (meV)	$\Gamma_0 \text{ (meV)}$	$\theta_{B_{\Gamma}}(K)$
E_1^{a}	2.32 ± 0.01	0.04 ± 0.01	176 ± 54	56±7	19 ± 10	276(f)
E_1 (Ref. 13)	2.33 ± 0.03	0.12 ± 0.04	360 ± 120	12 ± 9	25 ± 3	376(f)
E_1 (Ref. 14)	2.295 ± 0.002	0.063 ± 0.004	218 ± 14	11 ± 1	14.2 ± 0.3	218(f)
E_1 (Ref. 30)	2.292 ± 0.002	0.059 ± 0.003	198 ± 10	6 ± 2	25 ± 3	341 ± 34
$E_1 + \Delta_1^a$	2.52 ± 0.01	0.04 ± 0.02	165 ± 79	77 ± 8	19 ± 11	198(f)
$E_1 + \Delta_1$ (Ref. 13)	-	-	-	9 ± 8	43 ± 5	484(sic)
$E_1 + \Delta_1$ (Ref. 14)	2.494 ± 0.002	0.064 ± 0.001	218(f)	22 ± 3	15.1 ± 0.6	218(f)
$E_1 + \Delta_1$ (Ref. 30)	2.494 ± 0.002	0.064 ± 0.003	213 ± 9	14 ± 1	20(f)	250(f)

a Present work.

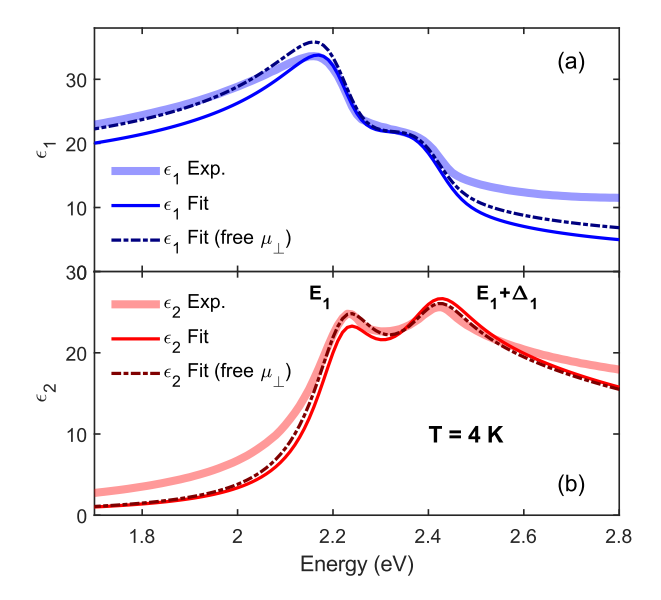


FIG. 5: Real (a) and imaginary (b) part of the dielectric function of Ge at 4 K. The translucent lines are the experimental data, the fitted model with masses from the $\mathbf{k} \cdot \mathbf{p}$ -model in Eqs. (12) is shown by the solid lines, and the model with the reduced mass as an additional free parameter is shown by the dot-dashed lines.

to the CB (Λ_6 -band) could be different than for the lh-band (Λ_6 -band). This would lead to different values of $k_{\rm max}$ for E_1 and $E_1 + \Delta_1$. Moreover, with increasing temperature, the bands renormalize and change their curvature slightly, which would ultimately result in a different value of $k_{\rm max}$ at each temperature. As the temperature increases, the agreement in the amplitude of the model and experiment improves for both CPs (see Fig. 6). This could be explained by the temperature dependence of $k_{\rm max}$. Nevertheless, a different $k_{\rm max}$ value for E_1 and $E_1 + \Delta_1$ is likely to have a small effect, considering how similar the hh and lh bands are to each other near the L-point.

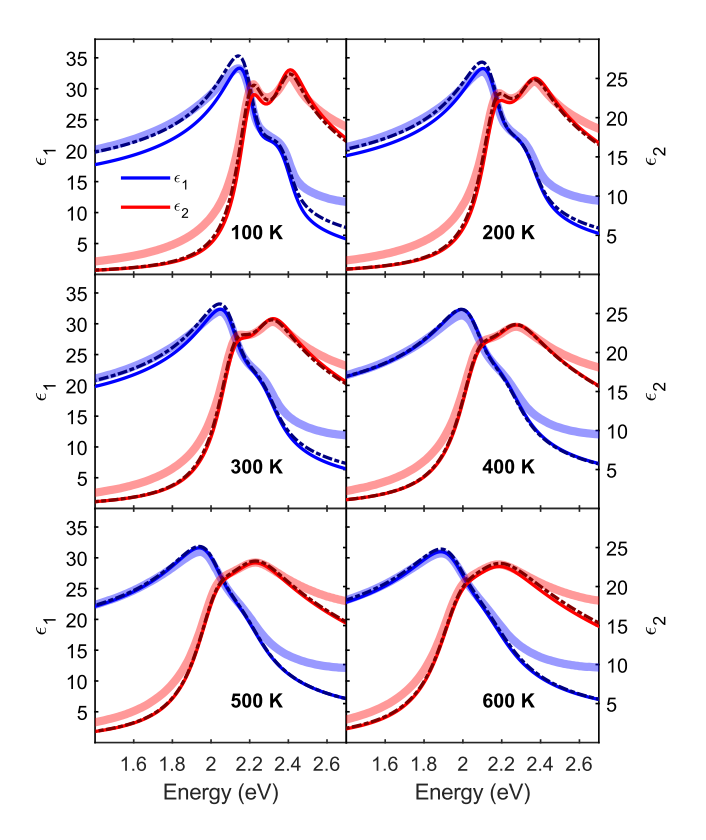


FIG. 6: Dielectric function of Ge from 100 to 600 K. The translucent lines are the experimental data, the fitted model from the $\mathbf{k} \cdot \mathbf{p}$ -model in Eqs. (12) is shown by the solid lines, and the model with the reduced mass as an additional free parameter by the dot-dashed lines.

D. Fitting the effective mass

A bigger factor in the disagreement between model and experiment could be the calculated reduced masses. The amplitudes in Eqs. (17) are only valid in the 6-band $\mathbf{k} \cdot \mathbf{p}$ -theory model at the L-point, where the reduced masses are given by Eq. (12). We resort to this definition of the masses in the absence of any known values for the hh and lh effective masses.

For the standard definition of the reduced mass,

$$\frac{1}{\mu_{\perp}^{(E_1, E_1 + \Delta_1)}} = \frac{1}{m_{\perp}^{(L_6^+)}} + \frac{1}{m_{\perp}^{(L_4^- \oplus L_5^-, L_6^-)}},\tag{20}$$

the amplitudes of the DF in Eq. (16) revert to their original forms of Eq. (6). To improve the agreement between theory and experiment, we can treat the reduced masses for both CPs as additional free parameters and refit our data. To avoid inconsistencies with the previously fitted values of broadening and energy, we divided the fitting process in two steps. Initially, to fit the broadening and energy, we performed a $2^{\rm nd}$ derivative fitting while holding the reduced masses constant and equal to their theoretical values. Subsequently, we fitted $\mu_{\perp}^{(E_1,E_1+\Delta_1)}$ and $\varepsilon_{\rm off}$ to the DF. If any discrepancies in their corresponding $2^{\rm nd}$ derivatives appeared between the model and experimental data, the two-step procedure was repeated until no further change was observed.

The effective masses obtained from this new fitting procedure can be seen in the dot-dashed lines of Figs. 5 and 6. Although the agreement between the model and the data improved significantly, there is no physical basis behind the fitted reduced mass values. Fig. 7 shows the fitted masses in comparison with the values calculated from Eq. (12). It also shows literature values of the reduced masses at 4 K^{7,51} and at room temperature. It can be seen that the difference between the fitted masses of the CPs is larger than in any reference. Furthermore, the fit suggests that the reduced mass for E_1 should be larger than the mass for $E_1 + \Delta_1$, which is not the case according to the literature values.

Nonetheless, it has been pointed out by Cardona that, in the Λ-direction, but not at the L-point, linear terms proportional to k_{\perp} in the bands tend to increase the reduced mass of E_1 while decreasing it for $E_1 + \Delta_1$. ^{13,54} This trend is also seen in Fig. 7. In our calculations, we used the masses at the L-point calculated from Eq. (12). However, this expression might not necessarily describe the masses in the k_{max} -region of the band structure (grey area in Fig. 1b). In this region, Cardona states that including linear k_{\perp} terms in the band structure would increase the reduced mass $\mu_{\perp}^{(E_1)}$. We would like to stress to the reader that, while the fitted reduced masses improve significantly the agreement between model and data, the strong temperature dependence seen in these fitted values should not be overinterpreted. As discussed, these masses serve purely as empirical parameters within the fitting procedure, and the effect of these linear terms in the reduced masses needs a more thorough study, perhaps in comparison with larger $\mathbf{k} \cdot \mathbf{p}$ models. In effect, this additional fitting parameter can be used to improve the agreement between model and data, but until further research clarifies the effects of additional terms in the reduced masses of these CPs, we are unable to justify this additional free parameter on theoretical grounds. Still, even without treating the masses as free parameters, we emphasize the excellent agreement between the theoretical model and the experimental data. Put another way, while the empirical fitting of the masses improves the match in the DF, it is not essential for obtaining remarkable results.

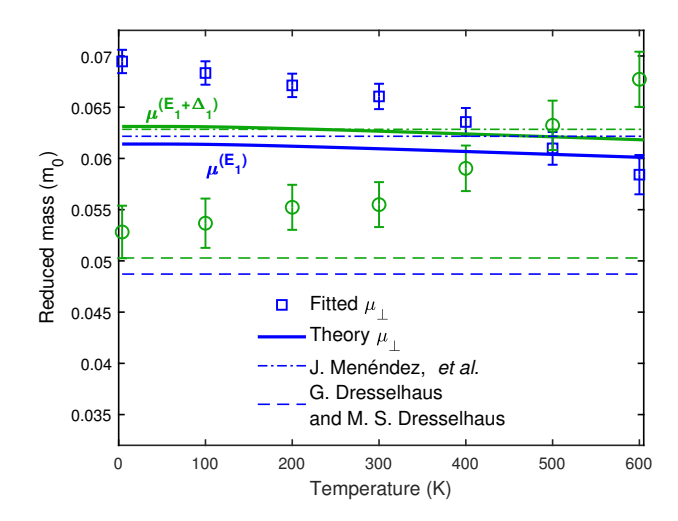


FIG. 7: Fitted reduced masses as a function of temperature for E_1 (\square) and $E_1 + \Delta_1$ (\bigcirc). The solid lines show results from Eqs. (12). The dot-dashed and dashed lines are literature values at 4 K^{7,51} and room temperature,⁵² respectively.

VI. DISCUSSION

One possibility for the difference between the measured and calculated DF is that near the energy of E_1 , there are interband transitions that do not occur along the Λ -direction of the Brillouin zone (in the Σ -direction, for example). While there is no CP present in this region, there is an energy separation between the CB and VB similar to the energy of E_1 . Depending on the strength of these additional absorption processes, they could affect the amplitude of each CP differently.

Additionally, surface effects could have an impact on the quality of the agreement between model and experiment. The physical and numerical removal of the oxide layer described in Sec. III has been proven to be effective previously.^{6,30,31} Hence, there is no reason to think that our point-by-point fit has large errors, or that temperature changes would affect this procedure significantly. Nonetheless, it is worth noting how this oxide layer affects the pseudo-DF $\langle \varepsilon \rangle$. As the oxide layer gets thicker, it tends to increase the amplitude of E_1 in $\langle \varepsilon_2 \rangle$, while leaving the amplitude of $E_1 + \Delta_1$ constant. In other words, an underestimation of the oxide layer thickness will give an E_1 amplitude greater than it should be in the extracted point-by-point fit for the substrate. Fig. 8 shows the DF of the point-by-point fit with different oxide layer thicknesses compared to our model. While the model resembles closer to the 30 Å oxide layer fit, the previously mentioned procedure to estimate the oxide thickness yielded a GeO₂ layer of 11 Å. Therefore there is no evidence from the fitting that this layer should be as thick as 30 Å. Hence, the match between our model and the overlayer fit seems to be purely coincidental. On the other hand, different surface orientations of the bulk Ge material lead to a different surface reconstructions, which also affects interband transitions due to the different lattice periodicity at the surface.⁵⁵ These effects, however, are too small

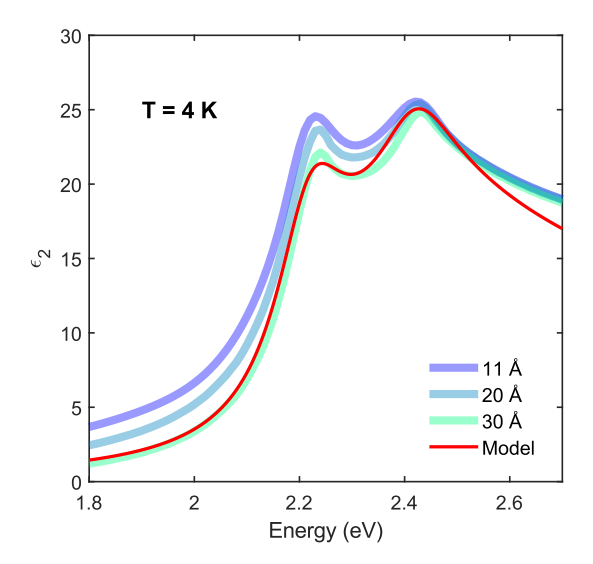


FIG. 8: Comparison between the model at 4 K (red solid line) and the point-by-point fits with different thicknesses for the oxide correction (translucent lines).

to make a difference in the discrepancies between our model and the experimental data (see supplementary material Sec. S6 for data differences depending on surface orientation).

Yet another factor to consider is excitonic screening. In the presence of excited electrons in the CB, the Coulomb interaction between the carriers gets partially screened. In his DF expression for three-dimensional excitons, Tanguy accounts for excitonic screening by solving the Schrödinger equation for the Hulthén potential. ⁵⁰ In contrast, such a solution for screened two-dimensional excitons does not exist in the literature. ^{58–61} For this reduced dimensionality problem, recent efforts have found the binding energy for screened excitons in two-dimensional materials (these are solutions to the Rytova-Keldysh potential). ^{56,57} Unfortunately, an expression of the DF for this potential is yet to be found. Moreover, given the low carrier densities at play, it is unlikely that including excitonic screening effects would improve our model.

Therefore, we conclude that the most probable sources of the difference between experiment and theory are nonresonant interband transitions and the precise values of the reduced masses of the CPs.

VII. CONCLUSION

In this work, we have demonstrated the importance of excitonic effects in the optical constants of Ge near the E_1 and $E_1 + \Delta_1$ CPs. By applying Tanguy's model for two-dimensional Wannier excitons, we provided an improved description of the DF that, despite not agreeing perfectly with the data, describes experimental results better than any efforts published so far. Furthermore, in the temperature characterization of the fitted CP parameters, our results show greater transition energies and broadenings due to the inclusion of ex-

citonic contributions.

Despite these advances, some discrepancies still persist in the amplitude of the CPs which require further revision of the theory. Specifically, future work should probe the effects of including linear k_{\perp} terms in the reduced masses of the CPs, the influence of remote bands, and potential contributions from nonresonant interband transitions. Moreover, extending this analysis to other semiconductor materials could help improve our calculations to refine the model even further.

SUPPLEMENTARY MATERIAL

See the supplementary material for a discussion of the parabolic approximation of the effective masses and how they are implemented to calculate the DF. Furthermore, a brief discussion of the unrenormalized masses and how they vary with temperature. We also discuss how the second derivatives are obtained numerically with the EG and SG digital filters. An analysis of the direct bandgap of Ge that includes non-parabolicity terms is presented as well. Finally, we discuss the impact of the surface orientation on the bulk DF.

ACKNOWLEDGMENTS

This material is based upon work supported by the Air Force Office of Scientific Research under award numbers FA9550-20-1-0135 and FA9453-23-2-0001. This material is based upon work supported by the Department of Energy, National Nuclear Security Administration under Award Number DE-NA0004103. This material is based upon work supported by the National Science Foundation under Award Number DMR-2423992. Contributions and discussions with José Menéndez are gratefully acknowledged. CAA gratefully acknowledges support from the J. A. Woollam Foundation.

AUTHOR DECLARATIONS

Conflict of Interest

The authors have no conflicts to disclose.

Author Contributions

Carlos A. Armenta: Conceptualization (lead); Formal analysis (lead); Investigation (lead); Methodology (lead); Software (lead); Visualization (lead); Writing – original draft (lead); Writing – review & editing (lead). **Stefan Zollner:** Project administration (lead); Supervision (lead); Validation (lead); Formal analysis (equal); Methodology (equal); Writing – review and editing (equal); Funding acquisition (lead).

Data Availability

The experimental data used in this study was previously published in Ref. 30 and is available therein. No new experimental data was generated for this work.

VIII. REFERENCES

- ¹P. Y. Yu and M. Cardona, Fundamentals of Semiconductors: Physics and Materials Properties (Springer, Berlin, 1996).
- ²M. Grundmann, *The Physics of Semiconductors* (Springer, Cham, Switzerland, 2021).
- ³J. I. Pancove, *Optical Processes in Semiconductors* (Dover, New York, 1971).
- ⁴R. J. Elliott, Phys. Rev. **108**, 1384 (1957).
- ⁵C. Tanguy, Phys. Rev. Lett. **75**, 4090 (1995).
- ⁶C. Emminger, N. S. Samarasingha, M. Rivero Arias, F. Abadizaman, J. Menéndez, and S. Zollner, J. Appl. Phys. 131, 165701 (2022).
- ⁷J. Menéndez, M. Noël, J. C. Zwinkels, and D. J. Lockwood, Phys. Rev. B 96, 121201 (2017); J. Menéndez, D. J. Lockwood, J. C. Zwinkels, and M. Noël, *ibid.* 98, 165207 (2018).
- ⁸J. Menéndez, C. D. Poweleit, and S. E. Tilton, Phys. Rev. B **101**, 195204 (2020)
- ⁹M. Dresselhaus, G. Dresselhaus, S. B. Cronin, and A. Gomes Souza Filho, *Solid State Properties* (Springer, Berlin, 2018).
- ¹⁰M. Cardona, in *Modulation Spectroscopy*, edited by F. Seitz, D Turnbull, and H. Ehrenreich (Academic, New York, 1969).
- ¹¹ J. E. Rowe and D. E. Aspnes, Phys. Rev. Lett. **25**, 162 (1970); **25** 979 (1970) (E).
- ¹²D. E. Aspnes, in *Handbook on Semiconductors*, edited by M. Balkanski (North-Holland, Amsterdam, 1980), Vol. 2, p. 109.
- ¹³L. Viña, S. Logothetidis, and M. Cardona, Phys. Rev. B **30**, 1979 (1984).
- ¹⁴N. S. Fernando, T. N. Nunley, A. Ghosh, C. M. Nelson, J. A. Cooke, A. A. Medina, S. Zollner, C. Xu, J. Menéndez, and J. Kouvetaskis, Appl. Surf. Sci. 421, 905 (2017).
- ¹⁵H. Fujiwara, Spectroscopic Ellipsometry: Principles and Applications (Wiley, Chichester, 2007).
- ¹⁶J. W. Garland, C. Kim, H. Abad, and P. M. Raccah, Phys. Rev. B 41, 7602 (1990).
- ¹⁷M. Cardona, in *Atomic Structure and Properties of Solids*, edited by E. Burstein (Academic Press, New York, 1972), p. 514.
- ¹⁸J. Humlíček and F. Lukeš, Phys. Stat. Solid. (b) **77**, 731 (1976).
- ¹⁹M. Rohlfing, Phys. Rev. B **82**, 205127 (2010).
- ²⁰B. A. Barker, J. Deslippe, J. Lischner, M. Jain, O. V. Yazyev, D. A. Strubbe, and S. G. Louie, Phys. Rev. B **106**, 115127 (2022).
- ²¹B. Cunningham, M. Grüning, D. Pashov, and M. van Schilfgaarde, Phys. Rev. B 108, 165104 (2023).
- ²²M. Shinada and S. Sugano, J. Phys. Soc. Jpn. 21, 1936 (1966).
- ²³R. Zimmermann, Jpn. J. Appl. Phys. **34**, 228 (1995).
- ²⁴C. Tanguy, Solid State Commun. **98**, 65 (1996).
- ²⁵C. Xu, N. S. Fernando, S. Zollner, J, Kouvetakis, and J. Menéndez, Phys. Rev. Lett. **118**, 267402 (2017).

- ²⁶C. Xu, J. Kouvetakis, and J. Menéndez, J. Appl. Phys. 125, 085704 (2019).
- ²⁷S. Espinoza, S. Richter, M. Rebarz, O. Herrfurth, R. Schmidt-Grund, J. Andreasson, and S. Zollner, Appl. Phys. Lett. 115, 052105 (2019).
- ²⁸C. Emminger, S. Espinoza, S. Richter, M. Rebarz, O. Herrfurth, M. Zahradník, R. Schmidt-Grund, J. Andreasson, S. Zollner, phys. stat. solidi RRL 16, 220058 (2022).
- ²⁹C. A. Armenta, M. Zahradnik, C. Emminger, S. Espinoza, M. Rebarz, S. Vazquez-Miranda, J. Andreasson, and S. Zollner, 2024 IEEE Photonics Society Summer Topicals Meeting Series (SUM), Bridgetown, Barbados, 2024, pp. 01-02.
- ³⁰C. Emminger, F. Abadizaman, N. S. Samarasingha, T. E. Tiwald, and S. Zollner, J. Vac. Sci. Technol. B 38, 012202 (2020).
- ³¹T. N. Nunley, N. S. Fernando, N. S. Samarasingha, J. M. Moya, C. M. Nelson, A. A. Medina, and S. Zollner, J. Vac. Sci. Technol. B 34, 061205 (2016).
- 32 See: https://www.jawoollam.com/
- ³³S. Flügge, *Rechenmethoden der Quantentheorie* (Springer, Berlin, 1965).
- ³⁴X. L. Yang, S. H. Guo, and F. T. Chan, Phys. Rev. A **43**, 1186 (1991).
- ³⁵K. A. Velizhanin and A. Saxena, Phys. Rev. B **92**, 195305 (2015).
- ³⁶T. Mueller and E. Malic, npj 2D Mater. Appl. **2**, 29 (2018).
- ³⁷W. C. Dunlap, Jr. and R. L. Watters, Phys. Rev. **92**, 1396 (1953).
- ³⁸F. A. D'Altroy and H. Y. Fan, Phys. Rev. **103**, 1671 (1956).
- ³⁹A. K. Sood, G. Contreras, and M. Cardona, Phys. Rev. B **31**, 3760 (1985).
- ⁴⁰Y. Ma and J. S. Tse, Solid State Commun. **143**, 161 (2007).
- ⁴¹G. Dresselhaus, A. F. Kip, and C. Kittel, Phys. Rev. **98**, 368 (1955).
- ⁴²S. Zollner, C. A. Armenta, S. Yadav, and J. Menéndez, J. Vac. Sci. Technol. A 43, 012801 (2025).
- ⁴³L. J. Bruner and R. W. Keyes, Phys Rev. Lett. **7** 55 (1961).
- ⁴⁴R. Zallen and W. Paul, Phys. Rev. **155** 703 (1967).
- ⁴⁵N. W. Ashcroft and N. D. Mermin, *Solid State Physics* (Saunders, Philadelphia, 1976).
- ⁴⁶V. L. Le, T. J. Kim, Y. D. Kim, and D. E. Aspnes, J. Vac. Sci. Technol. B 37, 052903 (2019).
- ⁴⁷D. K. Hoffman, D. J. Kouri, E. Pollak, Comput. Phys. Commun. **147**, 759 (2002).
- 48 See: https://www.mathworks.com/
- ⁴⁹A. Savitzky and M. J. E. Golay, Anal. Chem. **36**, 1627 (1964).
- ⁵⁰C. Tanguy, Phys. Rev. B **60**, 10660 (1999).
- ⁵¹J. Menéndez (private communication).
- ⁵²G. Dresselhaus and M. S. Dresselhaus, Phys. Rev. **160**, 649 (1967).
- ⁵³D. E. Aspnes, Phys. Rev. B **12** 2297 (1975).
- ⁵⁴M. Cardona, Phys. Rev. B **15** 5999 (1977).
- ⁵⁵M. K. Kelly, S. Zollner, M. Cardona, Surf. Sci. **285**, 282 (1993).
- ⁵⁶M. R. Molas, A. O. Slobodeniuk, K. Nogajewski, M. Bartos, Ł. Bala, A. Babiński, K. Watanabe, T. Taniguchi, C. Faugeras, and M. Potemski, Phys. Rev. Lett. **123**, 136801 (2019).
- ⁵⁷H. T. Nguyen-Truong, Phys. Rev. B **105**, L201407 (2022).
- ⁵⁸F. Stern and W. E. Howard, Phys. Rev. **163**, 816 (1967).
- ⁵⁹D. G. W. Parfitt and M. E. Portnoi, Physica E **17**, 212 (2003).
- ⁶⁰D. G. W. Parfitt and M. E. Portnoi, in *Mathematical Physics, Proceedings of the XI Regional Conference, Tehran, Iran, 3-6 May 2004* (World Scientific, Singapore, 2005), p. 52.
- ⁶¹A. J. Makowski, Phys. Rev. A **84**, 022108 (2011).

Supplementary Material: Excitonic effects at the temperature-dependent E_1 and $E_1 + \Delta_1$ critical points of Ge

(*Electronic mail: cobhc14@nmsu.edu.)

(Dated: 1 June 2025)

Carlos A. Armenta* and Stefan Zollner

Department of Physics, New Mexico State University, Las Cruces, NM 88003-8001, USA

S1. EFFECTIVE MASSES

A. Parabolic approximation at the L-point

The E_1 and $E_1 + \Delta_1$ critical points (CPs) presented in Fig. 1b arise from interband transitions taking place from the heavy-hole ($L_4^- \oplus L_5^-$ -band) and light-hole (L_6^- -band) valence band (VB) to the L_6^+ conduction band (CB), respectively. The symmetries associated with these bands correspond to the set of wave function basis vectors^{1,17}

$$L_{6}^{+}: \qquad |Z\uparrow\rangle, |Z\downarrow\rangle,$$

$$L_{4}^{-} \oplus L_{5}^{-}: \qquad \frac{1}{\sqrt{2}}|X+iY\uparrow\rangle, \frac{1}{\sqrt{2}}|X-iY\downarrow\rangle,$$

$$L_{6}^{-}: \qquad \frac{1}{\sqrt{2}}|X+iY\downarrow\rangle, \frac{1}{\sqrt{2}}|X-iY\uparrow\rangle.$$
(S1)

Just like in Sec. II, the *z*-axis was chosen along the Λ -direction. In this basis, and with the aid of $\mathbf{k} \cdot \mathbf{p}$ theory, we can explicitly calculate the matrix $\langle u_{n0} | \mathbf{k} \cdot \mathbf{p} | u_{n'0} \rangle$ to get an expression for the effective masses of the bands (*n* is the index of the band). We note that the only non-zero momentum matrix elements are^{1,17}

$$-i\langle Z|p_x|X\rangle = -i\langle Z|p_Y|Y\rangle = \overline{P}.$$
 (S2)

Naturally, the states in (S1) with opposite spins will not couple. Hence, the 6-band $\mathbf{k} \cdot \mathbf{p}$ Hamiltonian will become a 3×3 matrix represented as follows: 1,17

$$\langle u_{n0} | \mathbf{k} \cdot \mathbf{p} | u_{n'0} \rangle = \begin{bmatrix} \langle L_6^+ | \mathbf{k} \cdot \mathbf{p} | L_6^+ \rangle & \langle L_6^+ | \mathbf{k} \cdot \mathbf{p} | L_4 \rangle & \langle L_6^+ | \mathbf{k} \cdot \mathbf{p} | L_6^- \rangle \\ \langle L_4 | \mathbf{k} \cdot \mathbf{p} | L_6^+ \rangle & \langle L_4 | \mathbf{k} \cdot \mathbf{p} | L_4 \rangle & \langle L_4 | \mathbf{k} \cdot \mathbf{p} | L_6^- \rangle \\ \langle L_6^- | \mathbf{k} \cdot \mathbf{p} | L_6^+ \rangle & \langle L_6^- | \mathbf{k} \cdot \mathbf{p} | L_4 \rangle & \langle L_6^- | \mathbf{k} \cdot \mathbf{p} | L_6^- \rangle \end{bmatrix}$$

$$= \begin{bmatrix} 0 & \frac{i\overline{P}}{\sqrt{2}} k_{\perp} & \frac{i\overline{P}}{\sqrt{2}} k_{\perp} \\ -\frac{i\overline{P}}{\sqrt{2}} k_{\perp} & 0 & 0 \\ -\frac{i\overline{P}}{\sqrt{2}} k_{\perp} & 0 & 0 \end{bmatrix}. \tag{S3}$$

Since the only matrix elements that are nonzero are perpendicular to $|Z\rangle$, the wave vector **k** reduces to k_{\perp} and the motion of the carriers gets restricted to a two-dimensional plane. The full Hamiltonian is given by 1,17

$$\mathcal{H}_{\mathbf{0}} + \tilde{\mathcal{H}}_{\mathbf{k}} = \begin{bmatrix} E_1 & \frac{i\hbar \overline{P}}{m_0 \sqrt{2}} k_{\perp} & \frac{i\hbar \overline{P}}{m_0 \sqrt{2}} k_{\perp} \\ -\frac{i\hbar \overline{P}}{m_0 \sqrt{2}} k_{\perp} & 0 & 0 \\ -\frac{i\hbar \overline{P}}{m_0 \sqrt{2}} k_{\perp} & 0 & -\Delta_1 \end{bmatrix}.$$
 (S4)

After diagonalizing the matrix (S4), we get the characteristic equation

$$\tilde{E}^{3} - (E_{1} - \Delta_{1})\tilde{E}^{2} - \left(E_{1}\Delta_{1} + \frac{\hbar^{2}\overline{P}^{2}k_{\perp}^{2}}{m_{0}^{2}}\right)\tilde{E} - \frac{\hbar^{2}\overline{P}^{2}k_{\perp}^{2}\Delta_{1}}{2m_{0}^{2}} = 0,$$
(S5)

where $\tilde{E} = E - \hbar^2 k^2 / 2m_0$ is the modified energy parameter introduced by Kane⁶² (where the kinetic energy of the free electron has been subtracted). For small values of k_{\perp} , we can solve Eq. (S5) perturbatively to get the 3 solutions (one for each band):^{7,51}

$$E_{\text{CB}} = E_1 + \frac{\hbar^2 k_{\perp}^2}{2} \underbrace{\left[\frac{1}{m_0} + \frac{E_P}{m_0} \left(\frac{1}{E_1} + \frac{1}{E_1 + \Delta_1} \right) \right]}_{1/m_{\perp}^{(L_6^+)}} \tag{S6}$$

$$E_{\rm hh} = \frac{\hbar^2 k_{\perp}^2}{2} \underbrace{\left(\frac{1}{m_0} - \frac{E_P}{m_0 E_1}\right)}_{1/m_{\perp}^{(L_4^- \oplus L_5^-)}} \tag{S7}$$

$$E_{\rm lh} = -\Delta_1 + \frac{\hbar^2 k_\perp^2}{2} \left[\frac{1}{m_0} - \frac{E_P}{m_0 (E_1 + \Delta_1)} \right]$$

$$(S8)$$

To simplify the notation, we have made the substitution $E_P = \overline{P}^2/m_0$. Systems of correlated electron-hole pairs generated at the L-point will have a transverse reduced effective mass:¹⁷

$$\mu_{\perp}^{(E_1)} = \left[\frac{1}{m_{\perp}^{(L_0^+)}} - \frac{1}{m_{\perp}^{(L_0^+ \oplus L_5^-)}} \right]^{-1} = \left[\frac{E_P}{m_0} \left(\frac{2}{E_1} + \frac{1}{E_1 + \Delta_1} \right) \right]^{-1}$$
 (S9)

and
$$\mu_{\perp}^{(E_1 + \Delta_1)} = \left[\frac{1}{m_{\perp}^{(L_6^+)}} - \frac{1}{m_{\perp}^{(L_6^-)}} \right]^{-1} = \left[\frac{E_P}{m_0} \left(\frac{1}{E_1} + \frac{2}{E_1 + \Delta_1} \right) \right]^{-1}$$
 (S10)

corresponding to the two CPs E_1 and $E_1 + \Delta_1$, respectively.

B. Non-parabolicity at the L-point with small spin-orbit interaction

Instead of approximating for small values of k_{\perp} , we can solve the characteristic Eq. (S5) exactly with Vieta's solution for a cubic equation. These solutions, however, are not useful for our purposes given that they cannot be inverted to get the density of states as a function of energy. Instead, we can use the small spin-orbit (SO) approximation by letting $\Delta_1 \to 0$. If we do this, the characteristic equation becomes

$$\tilde{E}^3 - E_1 \tilde{E}^2 - \frac{\hbar^2 k_{\perp}^2}{m_0} E_P \tilde{E} = 0, \tag{S11}$$

with one solution $\tilde{E}_{hh} = 0$, and the other two

$$\tilde{E}_{\text{CB,lh}} = \frac{E_1 \pm \sqrt{E_1^2 + 4\frac{\hbar^2 k_{\perp}^2}{m_0} E_P}}{2}.$$
 (S12)

We can expand the square roots in Eq. (S12) in k_{\perp}^2 to obtain

$$E_{\text{CB}} = E_1 + \frac{\hbar^2 k_{\perp}^2}{2m_0} + \frac{E_1}{2} \left(1 + \sqrt{1 + \frac{4\hbar^2 k_{\perp}^2}{m_0} \frac{E_P}{E_1^2}} \right) \approx E_1 + \frac{\hbar^2 k_{\perp}^2}{2m_0} \left(1 + \frac{E_P}{E_1} - \frac{\hbar^2 k_{\perp}^2}{2m_0} \frac{E_P^2}{E_1^3} + 2\frac{\hbar^4 k_{\perp}^4}{2m_0^2} \frac{E_P^3}{E_1^5} \right)$$
(S13)

$$E_{\rm lh} = \frac{\hbar^2 k_{\perp}^2}{2m_0} + \frac{E_1}{2} \left(1 - \sqrt{1 + \frac{4\hbar^2 k_{\perp}^2}{m_0} \frac{E_P}{E_1^2}} \right) \approx \frac{\hbar^2 k_{\perp}^2}{2m_0} \left(1 - \frac{E_P}{E_1} + \frac{\hbar^2 k_{\perp}^2}{2m_0} \frac{E_P^2}{E_1^3} - 2\frac{\hbar^4 k_{\perp}^4}{2m_0^2} \frac{E_P^3}{E_1^5} \right). \tag{S14}$$

FIG. S1 shows the bands of the exact solution, the parabolic, and the small SO approximation. The CB in the small SO approximation is almost identical to the 6-band solution. For the lh-band, the curvature of the small SO approximation is similar

to the exact solution, however, the parabolic approximation is in better agreement to the exact solution. On the other hand, even in the 6-band model solution, the hh-band shows the wrong curvature. The band seems almost flat, indicating a nearly infinite transverse mass. Cardona states that including non-parabolicity terms linear in k_{\perp} make the transverse reduce mass for E_1 infinite.⁵⁴ However, this is in the Λ -region (and not at the L-valley). Unfortunately, this solution does not resemble what we see in $\mathbf{k} \cdot \mathbf{p}$ -theory calculations with higher number of bands.²⁵ Further calculations probing not only the bottom of the L-valley, but also the Λ -direction away from the L-valley are needed.

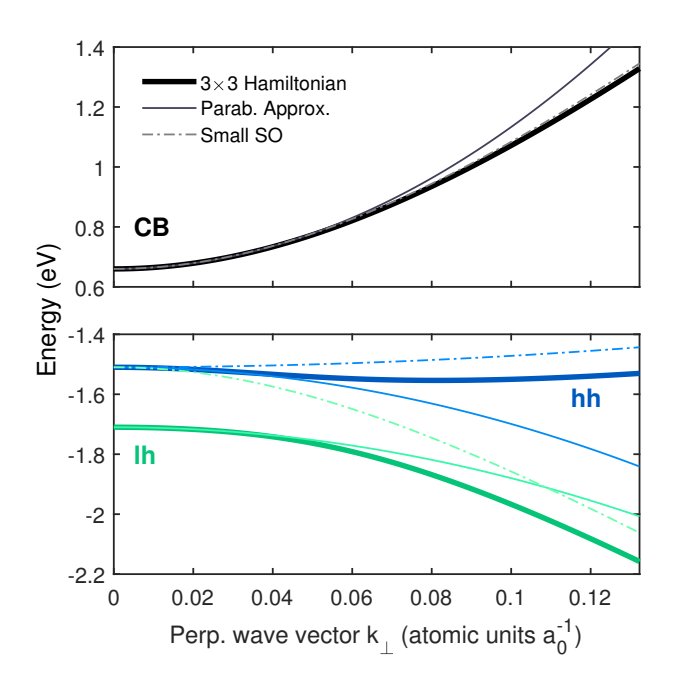


FIG. S1: Band structure of Ge at the L-valley. The perpendicular k_{\perp} -vector is shown in atomic units where $a_0 = 0.53$ Å. The thick solid lines represent the exact solution to the 3×3 Hamiltonian in Eq. (S4), the thin solid lines show the parabolic approximation, and the dot-dashed lines are the small spin-orbit approximation.

S2. DIELECTRIC FUNCTION OF GE

Previous attempts to describe the CPs of interest give the line shape of the DF as a step function 17

$$\varepsilon_2^{(E_1)} = \left(\frac{1}{4\pi\varepsilon_0}\right) \frac{16k_{\text{max}}e^2\overline{P}^2\mu_{\perp}^{(E_1)}}{3m_0^2E^2} H(E_1 - E), \tag{S15a}$$

$$\varepsilon_{2}^{(E_{1}+\Delta_{1})} = \left(\frac{1}{4\pi\varepsilon_{0}}\right) \frac{16k_{\text{max}}e^{2}\overline{P}^{2}\mu_{\perp}^{(E_{1}+\Delta_{1})}}{3m_{0}^{2}E^{2}}H(E_{1}+\Delta_{1}-E), \tag{S15b}$$

where H is the Heaviside step function, k_{max} is the maximum range in the k-axis where transitions take place, and \overline{P} is the average momentum matrix element. The real part ε_1 can be calculated from the expression for ε_2 with a Kramers-Kronig transformation. Alternatively, Humlíček gives the full expression for the DF while adding broadening to Eq. (S15) as 18

$$\varepsilon^{(E_1)}(E) = -\left(\frac{1}{4\pi\varepsilon_0}\right) \frac{16k_{\text{max}}e^2\overline{P}^2\mu_{\perp}^{(E_1)}}{3m_0^2\pi E^2} \ln\left[\frac{2(E_1 - i\Gamma - E)}{E_1 - i\Gamma}\right],\tag{S16a}$$

$$\varepsilon^{(E_1 + \Delta_1)}(E) = -\left(\frac{1}{4\pi\varepsilon_0}\right) \frac{16k_{\text{max}}e^2\overline{P}^2\mu_{\perp}^{(E_1 + \Delta_1)}}{3m_0^2\pi E^2} \ln\left[\frac{2(E_1 + \Delta_1 - i\Gamma - E)}{E_1 + \Delta_1 - i\Gamma}\right]. \tag{S16b}$$

Eqs. (S16) give the DF for uncorrelated electron-hole pairs shown by the blue dashed lines in Fig. 2.

In the following, we briefly describe how to derive Eq. (S15a). We start by computing the amplitude in Eq. (3) for the E_1 CP of Ge from the expression for the imaginary part of the dielectric tensor^{1,63}

$$\varepsilon_{2}(E)^{\mu\nu} = \left(\frac{1}{4\pi\varepsilon_{0}}\right) \frac{4\pi^{2}e^{2}\hbar^{2}}{m_{0}^{2}E^{2}} \sum_{CV} \langle V|p_{\mu}|C\rangle \langle C|p_{\nu}|V\rangle \int \frac{d\mathbf{k}}{4\pi^{3}} \delta(E_{C}(\mathbf{k}) - E_{V}(\mathbf{k}) - \hbar\omega). \tag{S17}$$

Since we are dealing with a cubic system, only the diagonal components of the tensor are non-zero. Therefore, we can replace the dielectric tensor with the dielectric function by averaging the contributing components $\varepsilon_2 = (\varepsilon_{xx} + \varepsilon_{yy} + \varepsilon_{zz})/3$. Moreover, from $\mathbf{k} \cdot \mathbf{p}$ theory, the matrix elements reduce to 17

$$\sum_{CV} \langle V | p_{\mu} | C \rangle \langle C | p_{\nu} | V \rangle = \underbrace{\left| \langle C | P_{x} | V \rangle \right|^{2}}_{\overline{P}^{2}/2} + \underbrace{\left| \langle C | P_{y} | V \rangle \right|^{2}}_{0} + \underbrace{\left| \langle C | P_{z} | V \rangle \right|^{2}}_{0} = \overline{P}^{2}, \tag{S18}$$

hence we can replace the matrix element in Eq. (S17) with the average transition matrix element \overline{P} . Finally, we multiply the DF by 4 to account for the L-valley degeneracy. The result is

$$\varepsilon_2(E) = \left(\frac{1}{4\pi\varepsilon_0}\right) \frac{4\pi^2 e^2 \hbar^2}{m_0^2 E^2} \left(\frac{4\overline{P}^2}{3}\right) \int \frac{d\mathbf{k}}{4\pi^3} \delta(E_{\mathcal{C}}(\mathbf{k}) - E_{\mathcal{V}}(\mathbf{k}) - \hbar\omega). \tag{S19}$$

To solve the integral in Eq. (S19), we replace it with the JDOS in Eq. (2) and switch to cylindrical coordinates. In the new coordinate system, the DF looks like

$$\varepsilon_{2}(E) = \left(\frac{1}{4\pi\varepsilon_{0}}\right) \frac{16\pi^{2}e^{2}\overline{P}^{2}\hbar^{2}}{3m_{0}^{2}E^{2}} \iiint \frac{k_{\rho}dk_{\rho}dk_{\varphi}dk_{z}}{4\pi^{3}} \delta\left(E_{1} + \frac{\hbar^{2}k_{\rho}^{2}}{2\mu_{\perp}} - E\right). \tag{S20}$$

The integral $\int dk_{\varphi} = 2\pi$ is trivial. To integrate over k_{ρ} , we make the substitution $u = \hbar^2 k_{\rho}^2/2\mu_{\perp}$, which transform the integral

$$\int_0^\infty k_\rho dk_\rho \, \delta\left(E_1 + \frac{\hbar^2 k_\rho^2}{2\mu_\perp} - E\right) \to \frac{\mu_\perp}{\hbar^2} \int_0^\infty du \, \delta\left(E_1 + u - E\right). \tag{S21}$$

Its solution yields the Heaviside step function $H(E_1 - E)$. Finally, the integral over k_z needs to be limited to the range where the transitions take place. We call this k_{max} . The final result for E_1 is

$$\varepsilon_2^{(E_1)} = \frac{A}{E^2} H(E_1 - E), \text{ with } A = \frac{4e^2 \overline{P}^2 \mu_{\perp}^{(E_1)}}{3\pi \varepsilon_0 m_0^2} k_{\text{max}},$$
(S22)

which is simply Eq. (S15a). Notice the similarity between the amplitudes in Eq. (S22) and Eq. (4a). These amplitudes are the same if we simply replace the transition matrix element $\mathbf{e} \cdot \mathbf{M}_{\text{CV}} \to \overline{P}^2 k_{\text{max}}/3$ and multiply by the valley degeneracy (multiply by 4 for L-valley).

S3. UNRENORMALIZED ENERGIES

To get the unrenormalized energies of the CPs, we will follow the procedure by Zollner *et al.*⁴² where they give the unrenormalized value for the direct bandgap E_0 as

$$E_0^u(T) = E_0^u(T = 0 \text{ K}) - 3B \left(\frac{\partial E_0^{\text{exp}}}{\partial p}\right)_T \int_0^T \alpha(\theta) d\theta, \tag{S23}$$

where the superscript u stands for unrenormalized, B is the bulk modulus, $\alpha(T)$ is the temperature-dependent thermal expansion coefficient, and p is the pressure. For our purposes, we will replace the unrenormalized energy at zero temperature with the fitted parameter E_a in the Bose-Einstein model of Eq. (15). The fitted parameters E_a , E_b , and θ_B in Table I are obtained by fitting the experimental CP energies of Table SI. Fig. S2 (b) shows the experimental energy of the E_1 and $E_1 + \Delta_1$ CPs as a function of temperature (dot-dashed lines). To subtract the thermal effect, we use the thermal expansion coefficient given by Eq. (14). Menéndez et al. obtained the values in Eq. (8) by fitting the experimental thermal expansion data from Ma and Tse. ⁴⁰ As

an alternative to Eq. (8), we could also use a more sophisticated expression for the thermal expansion coefficient provided by Roucka *et al.* as⁶⁴

$$\alpha(T) = \frac{4k_{\rm B}}{a_0^3 B} \left[\frac{2}{3} \gamma_{\rm TA} \left(\frac{\Theta_{\rm TA}}{T} \right)^2 \frac{e^{\Theta_{\rm TA}/T}}{\left(e^{\Theta_{\rm TA}/T} - 1 \right)^2} + \gamma_{\rm LA} \left(\frac{T}{\Theta_{\rm LA}} \right)^3 \int_0^{\Theta_{\rm LA}/T} \frac{x^4 e^x}{\left(e^x - 1 \right)^2} dx + \gamma_{\rm opt} \left(\frac{\Theta_{\rm opt}}{T} \right)^2 \frac{e^{\Theta_{\rm opt}/T}}{\left(e^{\Theta_{\rm opt}/T} - 1 \right)^2} \right], \quad (S24)$$

where $a_0 = 5.6568$ Å is the lattice constant, 65 γ is the Grüneisen parameter, and Θ is the Debye temperature. The subscripts LA, TA, and opt stand for the longitudinal acoustic, transverse acoustic, and optical modes, respectively. As seen in Fig. S2 (a), the more complicated expression in Eq. (S24) yields an almost identical result to Eq. (14). Therefore, we settle on using Eq. (8) for this work. Fig. S2 (a) also shows experimental thermal expansion coefficients from the literature. 66,67

The result of the unrenormalized energy in Eq. (S23) is shown in Fig. S2 (b) (solid lines). For this calculation, we take the value of $(\partial E_1/\partial p)_T \approx [\partial (E_1+\Delta_1)/\partial p]_T$. We justify this assumption by noting that the SO shift Δ_1 is related to atomic effects and it is, for the most part, unaffected by the distance of the atoms within the lattice. Finally, Fig. S2 (c) shows the exciton binding energies for both CPs in the left axis (solid lines), as well as the reduced masses on the right axis (dashed lines).

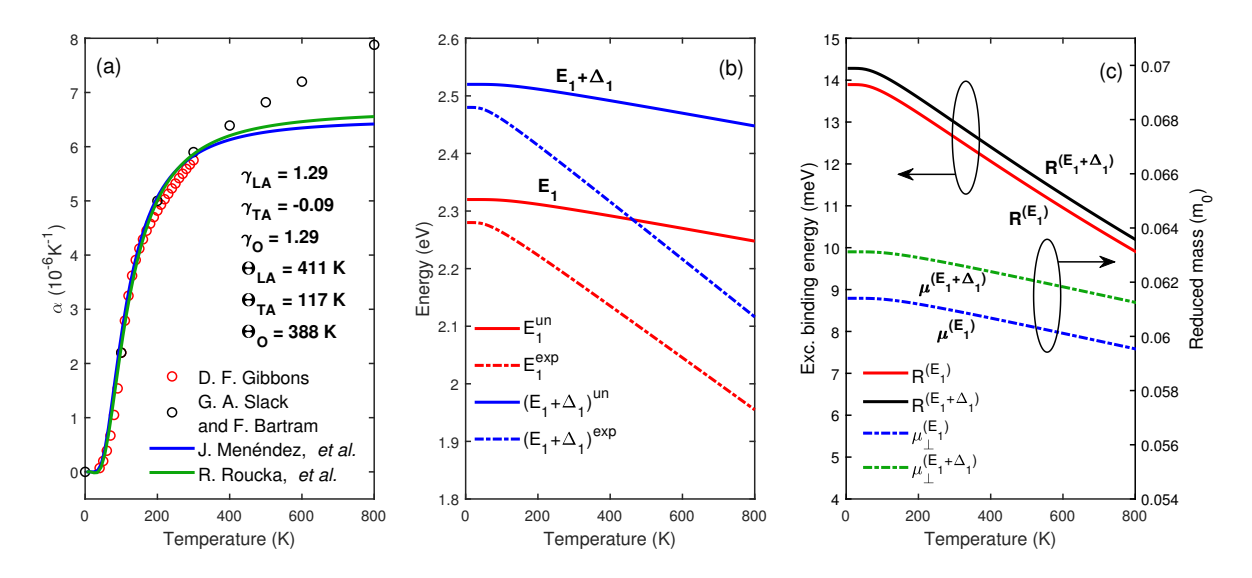


FIG. S2: (a) Thermal expansion coefficient from Eq. $(14)^{36}$ (blue solid line) and Eq. $(S24)^{64}$ (green solid line) compared to experimental data (\bigcirc) . 66,67 (b) The experimental values for E_1 and $E_1 + \Delta_1$ (blue and red dot-dashed line, respectively) are shown along with their respective unrenormalized energy (red and blue solid lines, respectively). (c) On the left axis is the binding energy of the excitons of the critical points (black and red solid lines). On the right axis is the transverse reduced effective masses (green and blue dot-dashed lines).

S4. FITTING PROCEDURE

To suppress the noise of the experimental data, we used a direct space convolution of the experimental DF with a digital filter. The convolution \overline{f} between f(x) and b(x) has the following property:

$$\overline{f}(x) = \int_{-\infty}^{\infty} \mathrm{d}x' f(x - x') b(x') = \int_{-\infty}^{\infty} \mathrm{d}x' f(x') b(x - x'). \tag{S25}$$

Note that, in light of Eq. (S25), operations such as $d\overline{f}(x)/dx$ produce the same outcome whether they act on f(x-x') or b(x-x'). To compute the second derivative of the experimental data, we take full advantage of this property by differentiating the digital filter (an analytical function) instead of the experimental data (a set of discrete points). To perform the convolution, we used MATLAB's built-in function conv(u,v), where u and v are the vectors being convoluted. For the fitting procedure, we created a residual vector function with five free parameters $[E_1, \Delta_1, \Gamma^{(E_1)}, \Gamma^{(E_1+\Delta_1)}]$, and ε_{off} . The two components of this vector function consisted of the real and imaginary part of the experimental 2^{nd} derivative of the DF minus the corresponding parts of

TABLE SI: Value of the fitting parameters and filter width ΔE for the extended Gauss digital filter. The step size selected was 1 meV from 1.0 to 3.2 eV (2201 points). (f) indicates a fixed parameter.

T	ΔE (meV)	<i>E</i> ₁ (eV)	$E_1 + \Delta_1 \text{ (eV)}$	$\Gamma^{(E_1)}$ (meV)	$\Gamma^{(E_1+\Delta_1)}$ (meV)	$arepsilon_{ m off}$
4 K	12.0	2.2793 ± 0.0009	2.4779 ± 0.002	75 ± 1	96±2	6(f)
100 K	14.5	2.2599 ± 0.0008	2.4600 ± 0.002	79 ± 1	103 ± 2	6(f)
200 K	17.5	2.2187 ± 0.0009	2.4176 ± 0.002	89 ± 1	119 ± 2	7(f)
300 K	21.5	2.1674 ± 0.0009	2.3638 ± 0.002	101 ± 1	136 ± 2	7(f)
400 K	27.5	2.1167 ± 0.0006	2.3147 ± 0.002	115 ± 1	157 ± 2	8(f)
500 K	27.5	2.0656 ± 0.0007	2.2642 ± 0.003	128 ± 1	175 ± 2	8(f)
600 K	25.0	2.0172 ± 0.0009	2.2170 ± 0.003	142 ± 1	193 ± 3	8(f)
700 K	33.0	1.968 ± 0.001	2.1683 ± 0.004	155 ± 1	212 ± 4	8(f)
800 K	35.0	1.917 ± 0.002	2.1182 ± 0.006	171 ± 2	243 ± 6	9(f)

TABLE SII: Value of the fitting parameters and order of polynomial n for the Savitzky-Golay digital filter. The frame length was constrain to 5% of the number of points (11 points). (f) indicates a fixed parameter.

T	n	<i>E</i> ₁ (eV)	$E_1 + \Delta_1 \text{ (eV)}$	$\Gamma^{(E_1)}$ (meV)	$\Gamma^{(E_1+\Delta_1)}$ (meV)	$arepsilon_{ m off}$
4 K	7	2.279 ± 0.002	2.478 ± 0.006	76 ± 3	96±6	6(f)
100 K	7	2.260 ± 0.002	2.460 ± 0.006	80 ± 2	103 ± 5	6(f)
200 K	7	2.219 ± 0.003	2.418 ± 0.005	89 ± 3	119 ± 7	7(f)
300 K	5	2.167 ± 0.003	2.364 ± 0.005	102 ± 2	137 ± 5	7(f)
400 K	5	2.117 ± 0.002	2.315 ± 0.005	116 ± 2	157 ± 6	8(f)
500 K	5	2.066 ± 0.002	2.264 ± 0.007	129 ± 2	175 ± 6	8(f)
600 K	4	2.017 ± 0.002	2.217 ± 0.008	142 ± 3	193 ± 9	8(f)
700 K	3	1.968 ± 0.003	2.17 ± 0.01	155 ± 3	212 ± 12	8(f)
800 K	3	1.917 ± 0.006	2.12 ± 0.02	171 ± 6	234 ± 18	9(f)

the numerical derivative of the model:

$$\operatorname{residual}(E_{1}, \Delta_{1}, \Gamma^{(E_{1})}, \Gamma^{(E_{1} + \Delta_{1})}, \boldsymbol{\varepsilon}_{\operatorname{off}}, E) = \begin{bmatrix} \operatorname{Re}\left\{\frac{\mathrm{d}^{2} \varepsilon^{\exp}(E)}{\mathrm{d}E^{2}}\right\} - \operatorname{Re}\left\{\frac{\mathrm{d}^{2} \varepsilon^{\operatorname{model}}(E_{1}, \Delta_{1}, \Gamma^{(E_{1})}, \Gamma^{(E_{1} + \Delta_{1})}, \boldsymbol{\varepsilon}_{\operatorname{off}}, E)}{\mathrm{d}E^{2}}\right\} \\ -\operatorname{Im}\left\{\frac{\mathrm{d}^{2} \varepsilon^{\exp}(E)}{\mathrm{d}E^{2}}\right\} - \operatorname{Im}\left\{\frac{\mathrm{d}^{2} \varepsilon^{\operatorname{model}}(E_{1}, \Delta_{1}, \Gamma^{(E_{1})}, \Gamma^{(E_{1} + \Delta_{1})}, \boldsymbol{\varepsilon}_{\operatorname{off}}, E)}{\mathrm{d}E^{2}}\right\} \end{bmatrix}. \tag{S26}$$

After creating the residual vector function (S26), we minimized it with the MATLAB function lsqnonlin(fun,x0,lb,ub), where the input fun is the function to be minimized, x0 is the vector with the initial guess for the fitting parameters, lb, and ub are the vectors with the lower and upper bounds for the fitting parameters, respectively.

A. Extended Gaussian digital filter

The extended Gaussian (EG) digital filter of Eq. (18) for M = 4 has the form 46,47

$$b_4(x) = \frac{1}{12288\Delta E\sqrt{\pi}} \left(15120 - \frac{10080x^2}{\Delta E^2} + \frac{1512x^4}{\Delta E^4} - \frac{72x^6}{\Delta E^6} + \frac{x^8}{\Delta E^8} \right) \exp\left(-\frac{x^2}{4\Delta E^2}\right). \tag{S27}$$

However, since we are interested in the 2^{nd} derivative of the data, we can compute the second derivative of Eq. (S27) and perform the convolution with $\varepsilon^{\exp}(E)$ afterward.

$$\frac{\mathrm{d}^2 b_4(x)}{\mathrm{d} x^2} = \frac{1}{49152 \Delta E^3 \sqrt{\pi}} \left(-110880 + \frac{188496 x^2}{\Delta E^2} - \frac{45936 x^4}{\Delta E^4} + \frac{3608 x^6}{\Delta E^6} - \frac{106 x^8}{\Delta E^8} + \frac{x^{10}}{\Delta E^{10}} \right) \exp\left(-\frac{x^2}{4 \Delta E^2} \right). \tag{S28}$$

To select the filter width ΔE , we Fourier-transform the experimental data and plot the natural logarithm of the amplitude C_n of the coefficients as seen Fig. S3 (a). We then eliminate the higher order coefficients (noise) and retain the lower ones which preserve the information of the original signal. The same cutoff of the coefficients is also applied to the Fourier transform of the EG filter $B_4(n)$, shown in Fig. S3 (a) as well. In this figure, we show the Fourier coefficients of the experimental data as a function of the order of coefficients n at 200 K, along with the Fourier transform of the extended Gaussian filter $B_4(n)$ for two different filter widths. For this particular measurement, we selected the cutoff at the 31st coefficient. The reader might find this

cutoff too conservative and that such a large filter width could suppress a portion of the signal. To address these concerns, we repeated the fitting procedure with the cutoff at the 41st coefficient [see the cyan dash-dotted line in Fig. S3 (a)]. We find that including higher-order coefficients increases noise but does not change the fitted energy and broadening parameters beyond their uncertainty. Therefore, we settled with the larger filter width. The dark circles in Fig. S3 (b) show the EG derivatives for this measurement. One of the advantages of this method is the increase in the number of points available in the derivative. In our case, the EG filter produces 2201 derivative points, resulting from the chosen energy step size of 1 meV over the range from 1.0 to 3.2 eV. This is in contrast to the Savitsky-Golay (SG) derivative [shown by the red and blue lines in Fig. S3 (b)], where the derivative is limited to the number of points of the original signal. Once the filter width has been selected, we can minimize the residual function in Eq. (S26) to fit the energy and broadening parameters. Table SI shows the fitted parameters for this method.

B. Savitzky-Golay digital filter

To obtain the SG digital filter, we employed the built-in MATLAB function sgolay(m,fl). This function gives a matrix of a finite impulse response smoothing filter. The input m is the polynomial order and fl is the frame length. We used 11 points for the frame length, which is approximately 5% of the total number of data points (this number must be odd). The order of the polynomial is listed in Table SII for each temperature series. Once we have generated the SG filter, we can obtain the n^{th} derivative by convolving the experimental data with the $(n+1)^{th}$ column of the filter matrix. The solid lines in Fig. S3 (b) show the SG derivatives for the experimental data at 200 K. Table SII shows the final values of the fitted parameters with the SG filter. Notice the similarity of the fitted values for energy and broadening between the two filters.

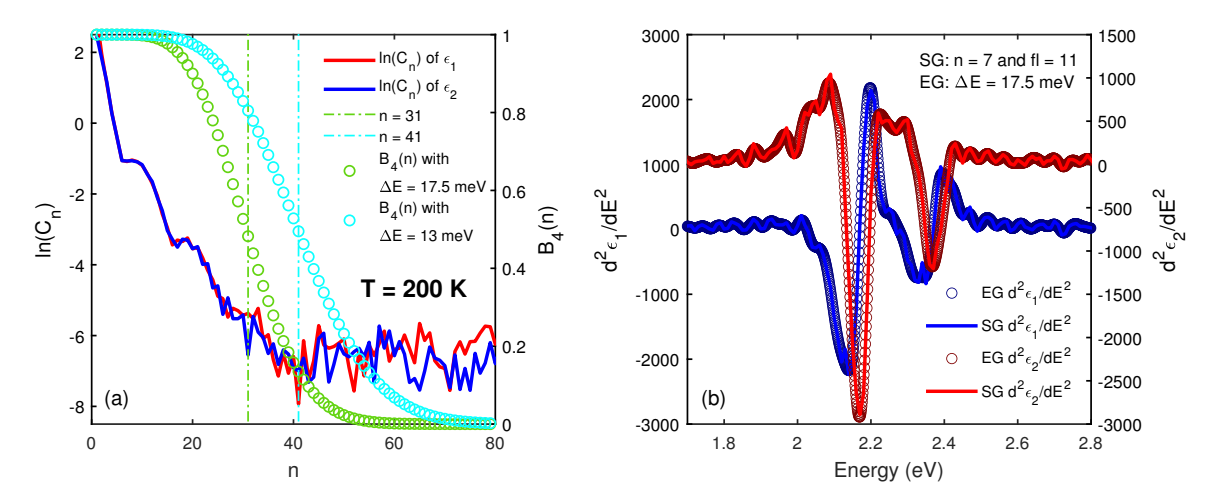


FIG. S3: (a) Natural logarithm of the Fourier coefficient amplitude C_n of the real (red) and imaginary (blue) parts of the dielectric function at 200 K. The same plot also shows the Fourier transform of the extended Gaussian filter (\bigcirc) for different filter widths. (b) 2^{nd} derivative of the dielectric function calculated with the extended Gauss filter (\bigcirc) and with the Savitzky-Golay filter (solid).

S5. DIRECT BANDGAP

The lineshape of the E_0 CP was presented previously by Emminger et al. as⁶

$$\varepsilon(E) = \frac{A\sqrt{R}}{\pi(E + i\Gamma)^2} \left\{ \tilde{g} \left[\xi(E + i\Gamma) \right] + \tilde{g} \left[\xi(-E - i\Gamma) \right] - 2\tilde{g} \left[\xi(0) \right] \right\}, \tag{S29}$$
 with $\tilde{g}(\xi) = -2\psi \left(\frac{g}{\xi} \right) - \frac{\xi}{g} - 2\psi (1 - \xi) - \frac{1}{\xi}, \ \xi(z) = \frac{2}{\sqrt{\frac{E_0 - z}{R}} + \sqrt{\frac{E_0 - z}{R}} + \frac{4}{g}}, \text{ and } A = \frac{e^2 \sqrt{m_0}}{\sqrt{2}\pi\varepsilon_0 \hbar^2} \mu_h^{3/2} \frac{E_P}{3}.$

This model is quite similar to Eq. (3), since it also takes into account excitonic (and screening) contributions to the CP. We can improve Eq. (S29) by including non-parabolicity contributions to the effective mass at the Γ -point. By following the procedure in Ref. 42 we use the small spin-orbit (SO) coupling approximation to get an analytical expression for the CB effective mass

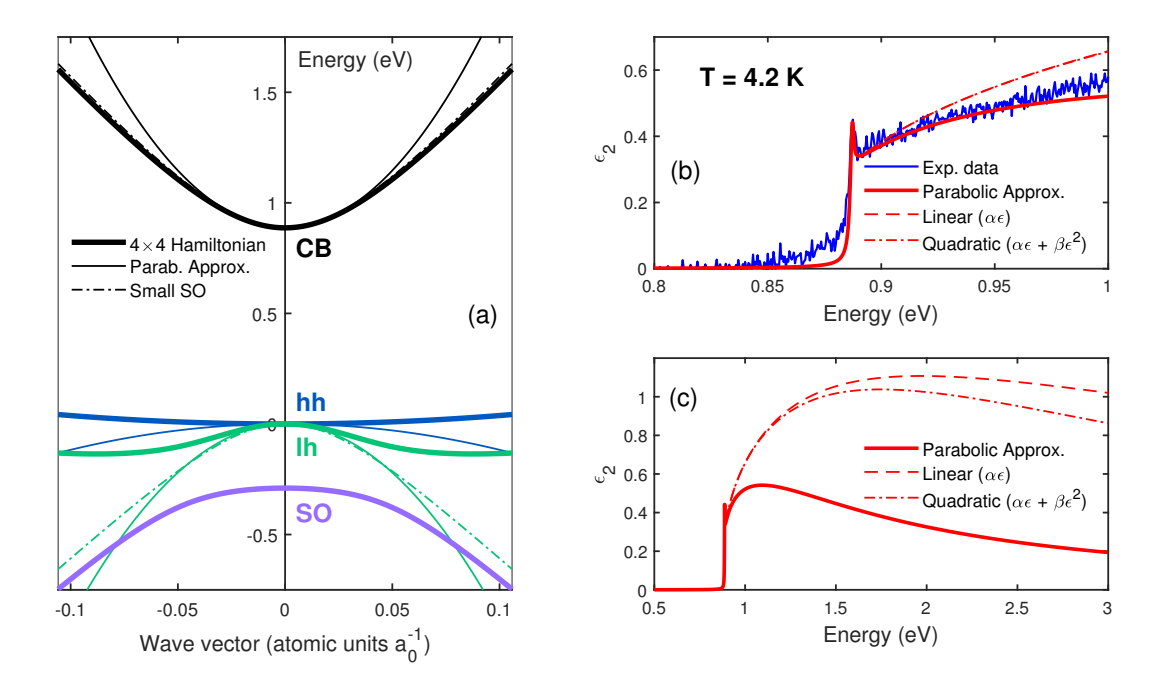


FIG. S4: (a) In addition to the parabolic approximation (thin solid line), we show the exact solution (thick solid line) and the small spin-orbit approximation (dot-dashed) to the 8-band model of the band structure of Ge. (b) Imaginary part of the dielectric function at 4 K in the parabolic approximation (solid) and including non-parabolicity linear terms in $\alpha\varepsilon$ (dashed) and quadratic terms in $\beta\varepsilon^2$ (dot-dashed) of the density of states mass. (c) Parabolic (solid) and non-parabolic (dashed, dot-dashed) models extended up to 3 eV.

and, therefore, the electron density of states (DOS) mass. If we consider an 8-band model (CB, hh, lh, and SO band), our $\mathbf{k} \cdot \mathbf{p}$ Hamiltonian looks like⁶²

$$\mathcal{H}_0 + \tilde{\mathcal{H}}_{\mathbf{k}} = \begin{bmatrix} E_0 & 0 & -\frac{\hbar k}{m_0} iP & 0\\ 0 & -\frac{2\Delta_0}{3} & \frac{2\Delta_0}{3} & 0\\ \frac{\hbar k}{m_0} iP & \frac{2\Delta_0}{3} & -\frac{2\Delta_0}{3} & 0\\ 0 & 0 & 0 & 0 \end{bmatrix}.$$
 (S30)

We can construct an exact solution of the band energies by solving the characteristic equation to this eigenvalue problem. Similar to Eq. (S5), the exact solutions to Eq. (S30) are not useful for our purposes because they cannot be inverted to get the DOS as a function of energy. Instead, we assume that the spin-orbit (SO) coupling is small and approximate $\Delta_0 \to 0$. As a result, this approximation makes the center terms in the Hamiltonian matrix (S30) zero and gives two degenerate solutions of zero (the hh-and SO-band) and two non-zero solutions (the CB and lh-band). In Fig. S4 (a), we can see that in the small SO approximation, the CB fits reasonable well to the exact solution of the band structure (at least in our 8-band 4×4 Hamiltonian model). Since there are two zero solutions in the small SO approximation, the hh- and SO-VB are degenerate and lie on top of the exact solution of the hh-band. The effective mass of the electron in CB and the hole in the lh-band are, therefore, given as

$$m_e = \frac{E_0}{E_P + E_0},$$
 $m_{\text{lh}} = \frac{E_0}{E_P - E_0}.$

However, the band structure in Fig. S4 (a) clearly shows that the small SO approximation does not present a good match with the exact solution of the lh-band. For this reason, we will only consider non-parabolicity effects in the CB, while leaving the VB in its parabolic approximation form. Hence, we will only consider m_e to calculate the DOS mass⁴²

$$m_{e,\text{DOS}} = m_e \left[(1 + \alpha_e \varepsilon + \beta_e \varepsilon^2) (1 + 2\alpha_e \varepsilon + 3\beta_e \varepsilon^2)^2 \right]^{1/3}, \tag{S31}$$

where⁴²

$$\alpha_e = \frac{E_P^2}{E_0(E_0 + E_P)^2},$$

$$\beta_e = -\frac{2E_P^3}{E_0(E_0 + E_P)^4},$$
(S32)

and ε is the energy above the band minimum E_0 . Including α and β into the DOS effective mass has the effect of overestimating ε_2 . This can be seen in Fig. S4 (b). To compensate this, we would have to consider the k-dependence of the matrix element E_P , which should bring ε_2 closer to the experimental value (we do not pursue this here). Still, independently of the approximation, the amplitude of ε_2 is around one between 1.5 and 3 eV. Therefore, including E_0 in the Tanguy line-shape would not be enough to match the experimental data in the E_1 and $E_1 + \Delta_1$ region.

S6. SURFACE EFFECTS

To showcase the dielectric function for different surface orientations, we measured Ge substrates with (100), (110), and (111) surface orientations. We then follow the procedure explained in Sec. III to remove the effects of the oxide layer from the data. The (110) surface orientation had an estimated oxide layer thickness of about 28 Å, whereas the (100) and (111) surfaces had a similar oxide layer thickness of about 25 Å. The resulting point-by-point fits are shown in Fig. S5. It can be seen that the difference between the samples is negligible. Therefore, we find it unlikely that these surface-related effects are responsible for the discrepancies between theory and experiment observed in our model for the dielectric function near the E_1 and $E_1 + \Delta_1$ CPs.

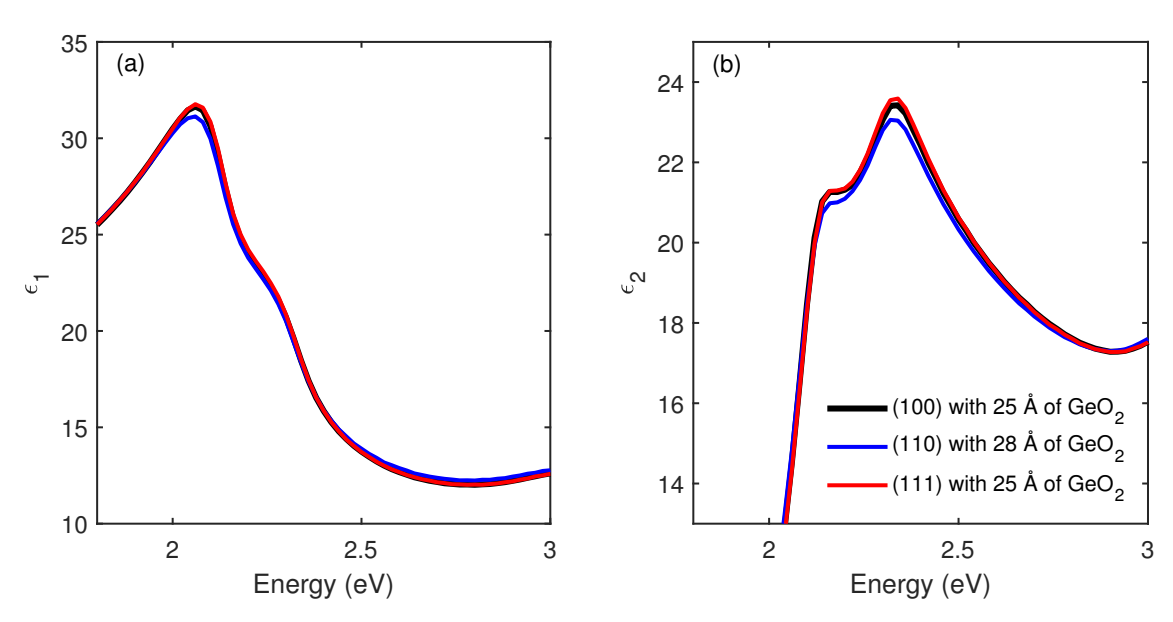


FIG. S5: Real (a) and imaginary (b) parts of the dielectric function of Ge from a point-by-point fit for three substrates with (100), (110), and (111) surface orientations (black, blue, and red, respectively).

ADDITIONAL REFERENCES

⁶² E. O. Kane, J. Phys. Chem. Solids **1**, 249 (1957).

³³ H. Kalt and C. F. Klingshirn, Semiconductor Optics 1: Linear Optical Properties of Semiconductors (Springer Nature Switzerland AG, 2019).

⁶⁴ R. Roucka, Y.-Y. Fang, J. Kouvetakis, A. V. G. Chizmeshya, and J. Menéndez, Phys. Rev. B **81** 245214 (2010).

⁶⁵ O. Madelung, *Semiconductors*, Landolt-Börnstein, New Series Vol. 41, Pt. A (Springer-Verlag, Berlin, New York, 2001).

⁶⁶ D. F. Gibbons, Phys. Rev. **112** 136 (1958).

⁶⁷ G. A. Slack, S. F. Bartram, J. Appl. Phys. **46**, 89 (1975).